

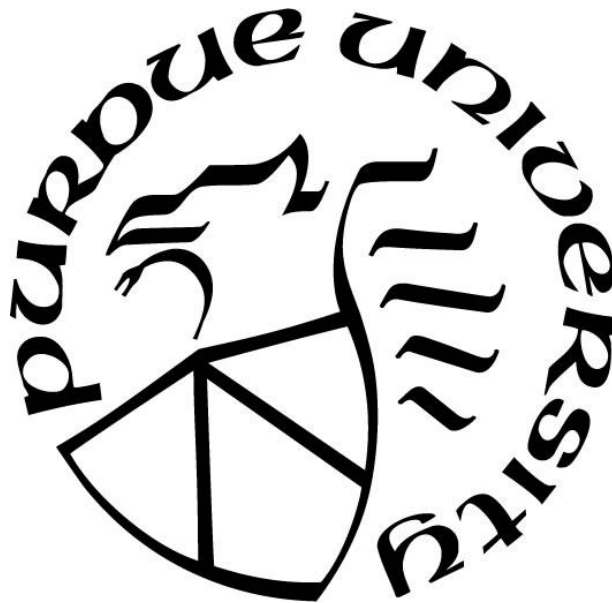
# **IN-VIVO QUANTIFICATION OF MAGNESIUM IN HAND BONE USING NEUTRON ACTIVATION ANALYSIS**

by  
**Colby Neumann**

**A Thesis**

*Submitted to the Faculty of Purdue University  
In Partial Fulfillment of the Requirements for the degree of*

**Master of Science**



School of Health Sciences

West Lafayette, Indiana

August 2019

**THE PURDUE UNIVERSITY GRADUATE SCHOOL**  
**STATEMENT OF COMMITTEE APPROVAL**

Dr. Linda Nie, Chair

School of Health Sciences

Dr. Keith Stantz

School of Health Sciences

Dr. Carlos Perez-Torres

School of Health Sciences

**Approved by:**

Dr. Aaron Bowman

Head of the Graduate Program

*To my parents, your support made this possible.*

## **ACKNOWLEDGMENTS**

Dr. Nie has been a wonderful mentor and advisor throughout these past couple of years. I am very grateful to have had the opportunity to be her student and she was instrumental in guiding me during this process. Dr. Nie's kindness and willingness to assist with any questions sets a great example, and I hope to emulate her passion towards her students.

I would also like to thank Dt. Stantz and Dr. Perez-Torres for their helpful comments about my research and their support for my future aspirations. Dr. Schweitzer, Matthew Tang, and Kyle Smith from Purdue's Radiological Environmental Management Group were very helpful in ensuring the safety of everyone in the laboratory. My lab teammates Mychaela Coyne, Michael Abel, Xinxin Zhang, Patrick Byrne, Sana Tabbassum, and Emma Wallens were wonderful to share a lab with. I am thankful for each and every one of you.

## TABLE OF CONTENTS

LIST OF TABLES .....	7
LIST OF FIGURES .....	8
ABSTRACT .....	10
CHAPTER 1. INTRODUCTION .....	11
1.1 Magnesium in the body .....	11
1.2 Techniques to measure magnesium .....	13
1.3 Neutron Activation .....	14
1.3.1 Neutron Activation Analysis of Magnesium .....	15
1.3.2 Monte Carlo Simulation of NAA .....	16
1.4 <i>In-Vivo</i> Neutron Activation Analysis .....	17
CHAPTER 2. SIMULATING NEUTRON ACTIVATION OF MAGNESIUM AND SIMULATING THE EFFICIENCY OF HPGE DETECTOR .....	18
2.1 Introduction .....	18
2.2 Material and Methods .....	19
2.2.1 Neutron Generator .....	19
2.2.2 HPGe .....	26
2.3 Simulation Results .....	28
2.3.1 Neutron Simulation Results .....	28
2.3.2 HPGe Results .....	33
2.4 Discussion .....	40
CHAPTER 3. IN-VIVO QUANTIFICATION OF MANGESIUM .....	43
3.1 Introduction .....	43
3.2 Materials and Methods .....	43
3.2.1 Constructing the magnesium phantom .....	43
3.3 Results .....	46
3.3.1 Fitting issue for multi-nuclide source .....	46
3.3.2 Phantom Results .....	48
3.3.3 Calibration Curve .....	50
3.3.4 Detection Limit .....	52

3.3.5 Dose .....	52
3.3.6 Discussion .....	53
CHAPTER 4. CONCLUSSION .....	55
REFERENCES .....	57
APPENDIX A. DETAILS OF SIMULATION AND EXPERIMENT PHANTOM CONCENTRATIONS .....	62
APPENDIX B. PHANTOM RECIPE.....	80

## LIST OF TABLES

Table 2.1 Example of Phantom Components .....	25
Table 2.2 Material Card for the 10,000 ppm Magnesium Phantom .....	32
Table 2.3 Activities of the Multi-Nuclide Source on the Day of Measurement .....	34
Table 2.4 Magnesium and Calcium Simulated Efficiencies Based on the Phantom Geometry ...	40
Table 3.5 Net Counts from the Phantom Irradiations .....	50
Table 3.6 The calculated Detection Limit of Magnesium for the Neutron Generator in this Work .....	52
Table A.1 Phantom recipe for all concentrations.....	80

## LIST OF FIGURES

Figure 1.1 Plot of ENDF/B-VII.1 neutron capture cross section in barns ( $10^{-24}$ cm) as a.....	15
Figure 2.1 Schematic of the DD109M Neutron Generator .....	19
Figure 2.2 Neutron Generator without the shielding .....	20
Figure 2.3 Example of a F4 Tally .....	22
Figure 2.4 Example of a Dose Tally in MCNP .....	24
Figure 2.5 HPGe Enclosed with Wrapped Lead and Records Gamma Counts .....	27
Figure 2.6 Neutron generator assembly in MCNP visualized with Visual Editor.....	28
Figure 2.7 HDPE surrounds the neutron generator. The cave marked by the black arrow indicates where the phantom is placed.....	29
Figure 2.8 Comparing the activation of magnesium for different moderators .....	30
Figure 2.9 Comparing the activation of magnesium normalized to the dose in 10 minutes.....	31
Figure 2.10 Simulated Calibration Curve .....	33
Figure 2.11 Comparing an Experimental and Simulated Multi-Nuclide Source.....	35
Figure 2.12 MCNP Efficiency Trials for the HPGe detector.....	36
Figure 2.13 HPGe Simulation Environment with a Multi-Nuclide Source .....	37
Figure 2.14 Comparing the multi-nuclide source geometry (left) and the phantom geometry (right). .....	38
Figure 2.15 Efficiency curve used to interpolate the magnesium efficiency.....	39
Figure 3.1 Failed magnesium phantom.....	44
Figure 3.2 10,000 ppm phantom with old phantom recipe .....	45
Figure 3.3 10,000 ppm phantom with new phantom recipe .....	46
Figure 3.4 1173 keV photon of Co60 from the standard multi-nuclide source. ....	47
Figure 3.5 Trying different function to fit the lower energy tail .....	48



Figure 3.6 Spectrum of an activated 10,000 ppm magnesium doped phantom with the  
magnesium and calcium peaks in the smaller boxes. .... 49

## ABSTRACT

Author: Neumann, Colby, R. MS

Institution: Purdue University

Degree Received: August 2019

Title: In-Vivo Quantification of Magnesium in Hand Bone using Neutron Activation Analysis

Committee Chair: Dr. Linda Nie

Magnesium is an essential element. An adult body contains approximately 21-28 grams of magnesium, with 50-60% present in the bones. Too high or too low levels of magnesium intake can have harmful effects on human body. To study how magnesium intake and storage in the body affect human health, it is important to identify a credible biomarker for the intake and storage. Usually, the amount of magnesium in the body is determined by a blood draw, but blood contains less than 1 percent of the total amount of magnesium in the body. In addition, the concentration of magnesium in blood is not stable. Bone holds the majority of magnesium in the body; therefore, bone is expected to be an ideal biomarker for measuring any surplus or deficiencies in the body. This thesis investigates the feasibility of quantifying magnesium in hand bone *in vivo* using MCNP simulation models and experiments with magnesium doped phantoms. The fast neutrons, generated by a deuterium-deuterium neutron generator with a flux of  $1\text{e}9$  neutrons/second, were moderated and guided to produce maximum number of thermal neutrons in an irradiation cave with acceptable radiation dose to the hand. The dimensions of the neutron generator along with the current shielding techniques were simulated in MCNP. The data show that the differences between the experimental and simulated calibration lines resulted in a percent difference of 9.40%. The experimental detection limit for bone magnesium was found to be  $334\text{ }\mu\text{g}$  magnesium/g dry bone with a total body dose of  $11\text{ }\mu\text{Sv}$ .

## CHAPTER 1. INTRODUCTION

### 1.1 Magnesium in the body

Magnesium is an essential element in the body and serves as a cofactor in more than 300 enzymatic reactions. Magnesium is the fourth most abundant cation in the body and second most abundant cation in intracellular fluid after potassium. It has been reported that 21-28 g of magnesium reside in the human body [1]. Bone contains the majority of magnesium in the body at 52.9%, muscle contains 27.0%, soft tissue contains 19.3%, erythrocytes contain 0.5% and blood serum contains 0.3% [2]. The concentration of magnesium in cortical bone for the reference man [3] is 2100 parts per million.

Magnesium is found in three different states in biological systems which include the ionized state, bound to complexed ions, and bound to protein. Only the ionized magnesium has biological activity and magnesium equilibrium is reached slowly between the tissue compartments [4]. The recommended intake of magnesium changes depending on a person's age and adults require more than adolescents. A male 30 years of age requires 400 mg/day and a female requires 310 mg/day [5]; however, all recommendations are based on a healthy individual. Magnesium is absorbed in the small and large intestine. The small intestine is referred to as the paracellular pathway and is responsible for the majority of magnesium absorption. The large intestine, specifically the cecum and colon, is referred to as the transcellular pathway [6]. While the intestines are the site of absorption, the kidneys are the main organ responsible for magnesium homeostasis [7]. Since the kidneys are responsible for magnesium homeostasis, there is clear dependence on what type of food is consumed. Magnesium can be found in grains, nuts, legumes, meat, and leafy vegetables because magnesium is the coordinating ion in chlorophyll.

Processed food reduces the magnesium content by 85% [8] and the popularization of processed food has reduced the magnesium intake for the general population. It's estimated 48% of Americans are deficient in magnesium due to processed food [9]. Magnesium plays an important role in stimulating osteoblasts in osteogenesis [10] and its deficiency leads to bone fragility and loss [11].

Hypomagnesemia occurs when the intestines or kidneys are not properly regulating the magnesium content in the body. Symptoms of hypomagnesemia can include nausea, fatigue, tremor, and cardiac arrhythmia [12]. Hypomagnesemia has also been associated with cardiovascular disease, diabetes mellitus type 2, and osteoporosis [13-16]. Hypermagnesemia is not as common as hypomagnesemia primarily due to the kidney being able to handle the increased concentration in the body. Hypermagnesemia can be caused when excess antacids or laxatives are administered, and the elderly are particularly susceptible because of reduced renal function [17]. Treatment of hypomagnesemia includes the administration of oral magnesium and treatment of hypermagnesemia includes ceasing administration of magnesium or haemodialysis [18]. Hypermagnesemia has shown to inhibit the action of the parathyroid hormone leading to hypocalcemia [19].

Magnesium plays a crucial role in maintaining the structure of DNA because it binds with the oxygen and nitrogen atoms in a polypeptide chain. Magnesium also binds the minor groove of DNA which protects it [6]. Since magnesium helps stabilize DNA, it's also necessary in the DNA and RNA polymerases. In a hypomagnesemia state, the DNA is more susceptible to radicals and oxidative stress. DNA and RNA polymerases are crucial in maintaining the integrity of DNA, so there is a chance of increased cancer risk in a hypomagnesaemia state as well. Magnesium acts as an antagonist to calcium and competes for nonspecific binding sites in the

muscle as well as inhibiting calcium release from the sarcoplasmic reticulum in response to increased extracellular calcium [20].

## **1.2 Techniques to measure magnesium**

Magnesium content in the body is measured using blood serum and blood accounts for less than one percent of the total magnesium content in the body. An individual may be in the normal reference range for serum magnesium content, but the overall magnesium content may be deficient [21]. Among the blood serum test, there are two additional tests that are used in the clinic. Serum ionized magnesium concentration is used in less than two percent of clinical laboratories in America suggesting clinicians value the total serum magnesium concentration and the other test is the measurement of magnesium excretion in urine during a 24 hour time period. Although the urine test can detect issues with kidney filtration, it does not quantify the magnesium content in the body [21]. Ion selective electrodes have been used to assess the extracellular magnesium but lacks selectivity [1]. Studies involving ICPMS, atomic emission spectrometry, and magnesium isotopes have investigated magnesium content [22-26].

Bone is an ideal biomarker to assess magnesium content in the body as it contains the majority of magnesium stored in the body. While blood may serve as a biomarker to assess acute changes, it's small concentration of magnesium would not be reliable in assessing progression of disease or understanding the status of magnesium content in the body. Magnesium is stored in hydroxyapatite portion of bone [27] and within this compartment, there are two pools of magnesium. One pool is readily exchangeable with extracellular material and accounts for 30% of bone magnesium and the other pool contains the remainder of magnesium which is not exchangeable [28]. A group has used neutron activation to assess magnesium content in the body using an accelerator based system [29], but some healthcare facilities may not have the space for

an accelerator; therefore, this work investigates a mobile and compact neutron activation system to quantify magnesium content in the body.

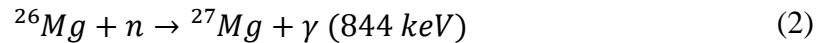
### 1.3 Neutron Activation

Neutron activation analysis (NAA) is a method to non-invasively quantify an element in any object. In NAA, a parent nuclide captures a thermal neutron which turns the nuclide to a radioactive nuclide. The parent nuclide will release a characteristic gamma ray as the element decays. These neutrons can come from a nuclear reactor, an accelerator, radionuclides, a deuterium-tritium (DT) reaction, or a deuterium-deuterium (DD) reaction. For in-vivo NAA, the neutrons need to be slowed using a moderator so they can interact with the object of interest. Water and graphite are the most common moderators in nuclear reactors because they have a low neutron absorption cross section. Low neutron absorption cross sections are essential for choosing moderators because the material needs to thermalize the neutrons without significantly absorbing the neutrons. The footprint of a reactor or accelerator limits the accessibility of NAA compared to using a DD reaction. A DD reaction can be incorporated into a compact and mobile system which increases the ability for subjects or objects to be tested when space is limited. NAA has been used to quantify materials in homeland security applications, soil, and even paintings [30-32].

For the DD reaction used in this work, neutron production is described by equation 1.



The neutrons can then be moderated and interact with an object producing a characteristic gamma ray. The neutron activation of magnesium is described in equation 2.



Where magnesium 26 is the parent nuclide and magnesium 27 is the produced radionuclide which gives rise to a characteristic gamma ray of 844 keV. The characteristic gamma rays are counted with either a NaI(Tl) detector or a high purity germanium (HPGe) detector. The HPGe detector offers superior resolution and can distinguish peaks with similar energies.

### 1.3.1 Neutron Activation Analysis of Magnesium

Magnesium 26 becomes activated from neutron capture and emits the magnesium 27 isotope. Magnesium 27 has a half-life equal to 9.45 minutes and emits three photons at 171, 844, and 1014 keV. The photons have an intensity of 0.84, 71.8%, and 28.0%, respectively [33]. Magnesium 26 has a thermal cross section equal to 39 mb [34] with the following characteristic cross section spectrum. Thermal neutrons lie in an energy range from  $1 \times 10^{-8}$  MeV to  $2 \times 10^{-7}$  MeV with a corresponding velocity of 2200 m/s.

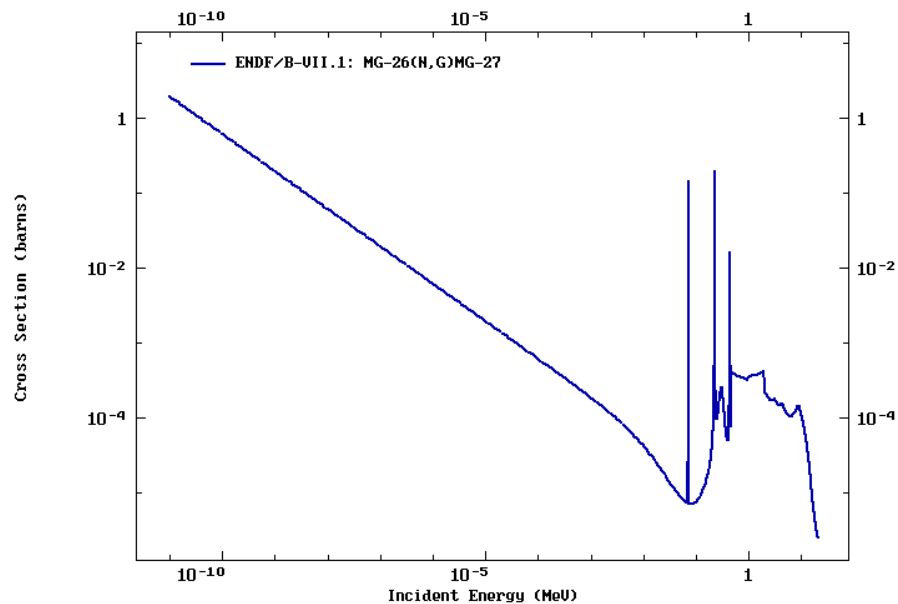


Figure 1.1 Plot of ENDF/B-VII.1 neutron capture cross section in barns ( $10^{-24}$  cm) as a function of neutron energy in MeV for magnesium [35]

### 1.3.2 Monte Carlo Simulation of NAA

#### 1.3.2.1 Irradiation

The simulation package used in this work was Monte Carlo N-Particle (MCNP) [36] developed at Los Alamos National Laboratory. The simulations were run on the RICE super computer cluster at Purdue University utilizing one node with two 10-core Xenon-E5 processors at 2.60 GHz. An input file for MCNP can be separated into three sections. The first section consists of creating cell definitions based on the surfaces that are defined in section two. The third section consists of many items and some of these items are material cards, source definition, the cell importance for a specific type of radiation, and tallies. A large number of particles ( $1e9$ ) was chosen for simulations to obtain results with an error that was less than five percent. Results with error greater than 5% are not considered.

This work focuses on NAA, and as a result, requires the use of the material modifier in MCNP. The material modifier is essential for simulations involving thermal neutrons. An example of this modifier looks like the following,

mt256 poly.10t

This line of the input file shows the modification of the material denoted as 256 in MCNP and it accesses the data in polyethylene library at room temperature to modify the hydrogen in this material. This tells MCNP to consider thermal neutron scatter and which is most prominent under 2 eV. MCNP uses the free gas treatment in simulations; however, when a material modifier is used as shown above, MCNP will use the data from the thermal libraries once energy values are available for the specific library. This is important for the neutron simulation because the energy of the neutrons can impact its interaction with other objects and considering the



thermal neutron scatter will make sure the simulation represents the interactions that are present in the experiment.

### ***1.3.2.2 $\gamma$ -Detection***

A HPGe detector was used to counts the gamma rays from the activated radionuclide. The detector system was simulated in MCNP to establish the efficiency of the detector for magnesium. The detector's efficiency for magnesium is essential to calculate the simulated net counts which can be used as a comparative tool for the experimental counts. A multi-nuclide source was used to find the experimental efficiency and then simulations were conducted. The geometry of the HPGe detector in the simulation was modified once the original simulated geometry proved to be a poor representation of the experiment.

## **1.4 *In-Vivo* Neutron Activation Analysis**

In vivo implies the use of a human subject when performing neutron activation analysis. For inanimate objects, dose isn't typically considered towards that object, but in general it still is important to adhere to the as low as reasonably achievable principle. For in-vivo studies involving living organism, it is essential to keep the dose as low as possible while maintaining the ability to obtain accurate and reliable data. To establish a max dose for the work in this study, the occupational dose limit for radiation workers (50 rem or 500 mSv) was used as a guideline. 10% of this dose or 5 rem (50 mSv) was the max dose set to the hand. The subject places their hand in the irradiation cave while the rest of their body is shielded. Previous studies involving this neutron generator have successfully quantified manganese, aluminum, and sodium [37-39].

## **CHAPTER 2. SIMULATING NEUTRON ACTIVATION OF MAGNESIUM AND SIMULATING THE EFFICIENCY OF HPGE DETECTOR**

### **2.1 Introduction**

This chapter reveals the efforts made to quantify magnesium in bone using in vivo neutron activation analysis. This process required two components: the construction and optimization of a HPGe detector in MCNP and the simulation of neutrons from a neutron generator colliding with magnesium doped hand phantoms. The radiation dose delivered to the phantom is one of the most important components for the simulation because too much dose has the potential to cause adverse side effects.

The detector simulation was used to establish a relationship between the energy and efficiency of a multi-nuclide source. Creating a simulation which represents the experimental efficiency values proves the simulation is an accurate representation of the experiment. This is essential because the multi-nuclide geometry is different than the phantom geometry and the phantom geometry is used in the simulation to create the efficiency curve allowing the efficiency of magnesium to be interpolated. There is no standard source with the geometry of the phantoms. So once the efficiency values from the simulation and experiment were similar, the geometry of the multi-nuclide was replaced with the phantom geometry. The neutron activation simulation allows for a comparison between experimental and simulated values which can be used to see if the experimental results are reasonable.

## 2.2 Material and Methods

### 2.2.1 Neutron Generator

#### 2.2.1.1 Generator Information

The neutron generator (DD109M) used in this work was manufactured at Adelphi Technologies. The generator utilizes a deuterium-deuterium (DD) reaction producing helium and neutrons with an energy of 2.45 MeV. The neutrons from the deuterium-deuterium reaction are thermalized and interacts with magnesium described by equation 2.

The deuterium gas will be ionized by a microwave source in the generator and an ion source will oxidize the deuterium so it can interact with the negative titanium target producing close to isotropic neutrons. Neutrons from this generator are produced at a rate of  $1 \times 10^9$  per second.

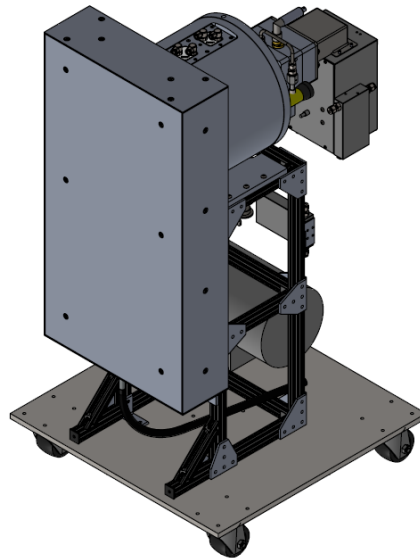


Figure 2.1 Schematic of the DD109M Neutron Generator

Figure 2.1 displays a 3D rendering the neutron generator in this work and this DD neutron generator was modelled in MCNP. Deuterium-deuterium and deuterium-tritium (DT)

neutron generators are popular mobile neutron generator options. The DD generator was preferred in this work for a couple reasons. It is much easier to shield a DD neutron generator compared to a DT generator because a DT generator will produce a higher energy neutron (14.1 MeV). Also, tritium used in the DT generator is radioactive; therefore, the neutron generator would need to be in an isolated system to ensure no leakage of tritium. The licensing to obtain and store tritium is more complicated than deuterium gas.

#### ***2.2.1.2 Irradiation Assembly***

The neutron generator is shielded by high density polyethylene (HDPE). There is an air gap shown in the rendering of the simulated neutron generator shown in figure 2.6 depicting a length of 40 cm from the reflector to the cylindrical portion of the generator. The space is mostly filled with wiring and tubes that connect the generator to the electronics rack, external cooler, and turbo. The phantoms are placed in the small cave near the center of the neutron output ensure maximum activation. Figure 2.2 shows the neutron generator without HDPE shielding and figure 2.6 was the simulated environment of the neutron generator.

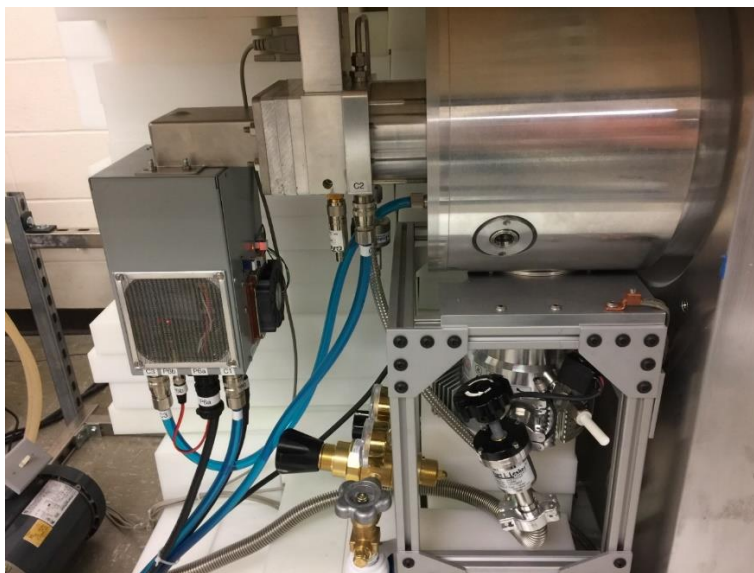


Figure 2.2 Neutron Generator without the shielding

### ***2.2.1.3 Monte Carlo Simulation***

#### ***2.2.1.3.1 Describing Input for HPGe and the Neutron Generator***

MCNP requires an input file created by the user. This input card needs to include creating geometries like a xy plane at a certain location and then cells can be created once enough geometries are created to make a desired shape. The user must also include a section where materials are defined by telling MCNP to use a set amount of an element in a compound, setting a radiation transport importance for each cell, indicating which type of particle will be simulated along with the source definition. The input cards I used for the neutron generator and HPGe detector are in appendix A. One of the common errors for a failed input file occurs when a cell is not properly defined leading to a significant portion of particles being lost. This issue can be visualized in MCNP's Visual Editor where red lines indicate a cell is not properly closed. The coordinates of the lost particles are in the output file and the user can input these coordinates into the Visual Editor to locate the issue.

#### ***2.2.1.3.2 Activating Magnesium***

The simulations in this work used the available materials cards in the Pacific Northwest National Laboratory (PNNL) material compendium [40]; however, the material cards for the magnesium phantoms were self-calculated because they are unique. The F4 tally in MCNP calculates the average flux over a cell. This parameter, in addition to the multiplier tally, is essential in simulating the activation of an element of interest in a cell. An example f4 tally is shown in figure 2.3.

```
f4:n 29
c e4:n 1e-8 100ILOG 2.5 $100i
fm4 2.858638E-04 308 102
sd4 1
```

Figure 2.3 Example of a F4 Tally

The first line in the figure above tells MCNP to only consider neutrons when averaging the flux across cell 29. The next line is a commented line where a logarithmic spectrum would be generated starting at an energy of  $1 \times 10^{-8}$  MeV and ending at 2.5 MeV with 100 bins between the starting and ending point. The sd4 option is incorporating the cell's volume into the algorithm for calculating the average flux over a cell. The modifier fm4 takes the following general shape,

$$fm4 \ c \ m \ r \quad (3)$$

c = Normalization factor usually in units of atom/barn-cm

m = Material number corresponding to the nuclide being activated

r = ENDF reaction number for radiative capture cross section (102)

The variable c changed depending on what concentration of magnesium that was simulated. It was calculated using equation 4.

$$c = \beta \frac{N_A b}{m} \quad (4)$$

$$\beta = (ppm * 10^{-6}) \frac{m_p}{V_p}$$

$N_A$  = Avogadro's number

b = conversion of  $\text{cm}^2$  to barns ( $1 \times 10^{-24}$ )

m = mass of the element being activated

$m_p$  = Mass of the phantom

$V_p$  = Volume of the phantom

At 10,000 ppm of magnesium, the fm4 calculation is below.

$$c = \frac{6.022 * 10^{23} \text{ mol}^{-1}}{26 \text{ g/mol}} * \frac{1 * 10^4 * 1 * 10^{-6} * 62 \text{ g}}{50.27 \frac{\text{g}}{\text{cm}^3}} * \frac{10^{-24} \text{ cm}^2}{\text{barn}} \quad (5)$$

$$= 2.858 * 10^{-4} \frac{\text{atom}}{\text{cm barn}}$$

To obtain the net counts from a simulation using the fm4 modifier for neutron activation, it requires an equation which accounts for the properties of the isotope of interest along with the irradiation protocol.

$$A = RN_o \Phi B_r I \varepsilon_E s d c \quad (6)$$

$A$  =  $\gamma$  gamma counts registered by the detector

$R$  = Reaction rate, which is an integration of neutron yield times cross section

$N_o$  = atom number for the target nuclide

$\Phi$  = Neutron flux measured in neutrons per second

$B_r$  = Branching ratio of the  $\gamma$ -ray for the radionuclide produced

$I$  = Abundance of the target nuclide

$\varepsilon$  = Efficiency of the HPGe at the excited  $\gamma$  energy

$s$  = Coefficient corresponding to the irradiation time

$$s = 1 - e^{-\lambda t_i} \quad (7)$$

Where  $t_i$  is equal to the irradiation time which was set to 10 minutes.

$d$  = Coefficient corresponding to the decay time

$$d = e^{-\lambda t_D} \quad (8)$$

Where  $t_D$  is equal to the decay time which was set to two minutes.

$c$  = Coefficient corresponding to the counting time measured in seconds.

$$c = \frac{1 - e^{-\lambda t_c}}{\lambda} \quad (9)$$

Where  $t_c$  is equal to the counting time which was set to two 15 minute intervals. Lambda represents the decay constant which is equal to the following,

$$\lambda = \frac{\ln(2)}{t_{1/2}} \quad (10)$$

Where  $t_{1/2}$  is equal to the half life of the radionuclide of interest.

The dose from activating magnesium was calculated using the df tally in MCNP. This tally is capable of providing a dose in either rem/h/source particle or Sv/h/source particle.

```
f14:n 29
df14 IU=2 IC=20
```

Figure 2.4 Example of a Dose Tally in MCNP

In figure 2.4, a separate tally is created to calculate the dose. IU=2 will provide the dose in Sv/h/source particle and IC=20 utilizes the dose function specified in NCRP 38 [41]. An in house dose limit is set to 50 mSv in 10 minutes when running an experiment. To convert the output of MCNP into a dose that can compared to the limit requires equation 11.

$$D = \frac{Sv \ s}{h \ n} \Phi \frac{1000 \ mSv}{1 \ Sv} \frac{1 \ hr}{60 \ min \ irradiation} \frac{10 \ min}{1} \quad (11)$$



$\Phi$ = Neutron flux measured in neutrons per second. The generator in this work is able to produce  $1 \times 10^9$  neutrons per second.

#### 2.2.1.3.3 Creating a calibration line

In both the simulation and experiment, magnesium doped phantoms were created. Four main compounds were used to create the phantoms: magnesium sulfate ( $\text{MgSO}_4$ ), calcium sulfate ( $\text{CaSO}_4$ ), ammonium chloride ( $\text{NH}_4\text{Cl}$ ), and sodium nitrate ( $\text{NaNO}_3$ ). The mass of calcium to be added in the recipe was varied to offset the increase in magnesium to maintain a total phantom mass of 62 grams. The mass of chloride and sodium were consistent in each phantom. As magnesium was added, calcium decreased and this decrease was calculated by subtracting the mass of chloride, sodium, and magnesium from 62 grams. The largest percentage change of calcium (between 0 and 10,000 ppm) was 5 percent. The fraction of magnesium, calcium, chloride, and sodium was taken from ICRP 23 [42] and then multiplied by the total mass of the phantom. This value is called the target mass which is then multiplied by the molar mass of the compound of interest (either  $\text{MgSO}_4$ ,  $\text{CaSO}_4$ ,  $\text{NaNO}_3$ , or  $\text{NH}_4\text{Cl}$ ) and then divided by the molar mass of the element of interest (either Mg, Ca, Na, or Cl). The following table includes the recipe used for 0 ppm. The remaining concentrations are in appendix B with the corresponding MCNP material cards.

Table 2.1 Example of Phantom Components

		Magnesium	Calcium	Chloride	Sodium
0 ppm	Target Mass	0	13.75 g	0.1736 g	0.3968 g
	Mass to be added to phantom	0	60.271 g	0.2619 g	1.467 g
	ppm/ $10^6$	0	0.226298	0.0028	0.0064

Creating a calibration line requires the net counts and concentration of each phantom. Ideally, the calibration line would have a perfect linear relationship. The concentration from an in-vivo study can be determined by using this calibration line. The counts from the experiment are plugged into the y component of the linear relationship and x is solved for. The variable x represents the concentration.

## 2.2.2 HPGe

### 2.2.2.1 Detector Information and Processing

The HPGe detector used in this work was designed and built by Ortec (AMETEK, OakRidge, TN). The specific model number is GMX100P4-95-A and this detector is quoted as having 100% efficiency. Maestro was used to collect the data from the HPGe and an in house program in MatLab was used to fit the Gaussian peaks from the sample. A Trust-Region algorithm was applied to the nonlinear least squares method in MatLab for the functions used to fit the peaks. The user needs to input a lower bound and upper bound of values for the coefficients in this method and then choose an initial starting point for each coefficient. Most of the peaks of interest were fit with the following equation,

$$y = Ae^{-0.5\left(\frac{x-B}{C}\right)^2} + D \quad (12)$$

Where A = amplitude of the peak, B is the energy of the peak of interest, C is the width of the peak, and D represents the background. However, it was necessary to include an error function in the equation above to fit peaks with high amount of counts; otherwise, the equation above would not adequately fit a portion on the lower energy side of the peak, and the motivation to include such a term in the fitting equation was from the work done by Jin et al [43]. The modified equation is,

$$y = Ae^{-0.5\left(\frac{x-B}{C}\right)^2} + D * \operatorname{erfc}\left(\frac{x-B}{C}\right) + E \quad (13)$$

Where E is equal to the background term.

#### 2.2.2.2 Counting Setup

After irradiation, the samples were placed flush with the HPGe cap depicted in figure 2.5. The lead bricks are wrapped with tape to prevent the spread of lead contamination, and the lead bricks also serve to reduce background radiation to increase the sensitivity of the HPGe detector.



Figure 2.5 HPGe Enclosed with Wrapped Lead and Records Gamma Counts

## 2.3 Simulation Results

### 2.3.1 Neutron Simulation Results

#### 2.3.1.1 Designing the Generator in MCNP

The neutron generator used in this work was modelled in MCNP based off figure 2.1. The experimental setup shown in figure 2.2 was measured with a tape measure so that the setup could be accurately designed in MCNP. Most of the shielding consisted of high density polyethylene (HDPE) on all sides of the generator with a small piece of lead in the irradiation cave where the phantom resides. The moderator, which is in between the neutron generator and the phantom, serves to slow down the fast neutrons so that they can interact and excite the object of interest. The other portions of the shielding serve as reflectors. These reflectors can both reflect and absorb neutrons to reduce the neutron dose.

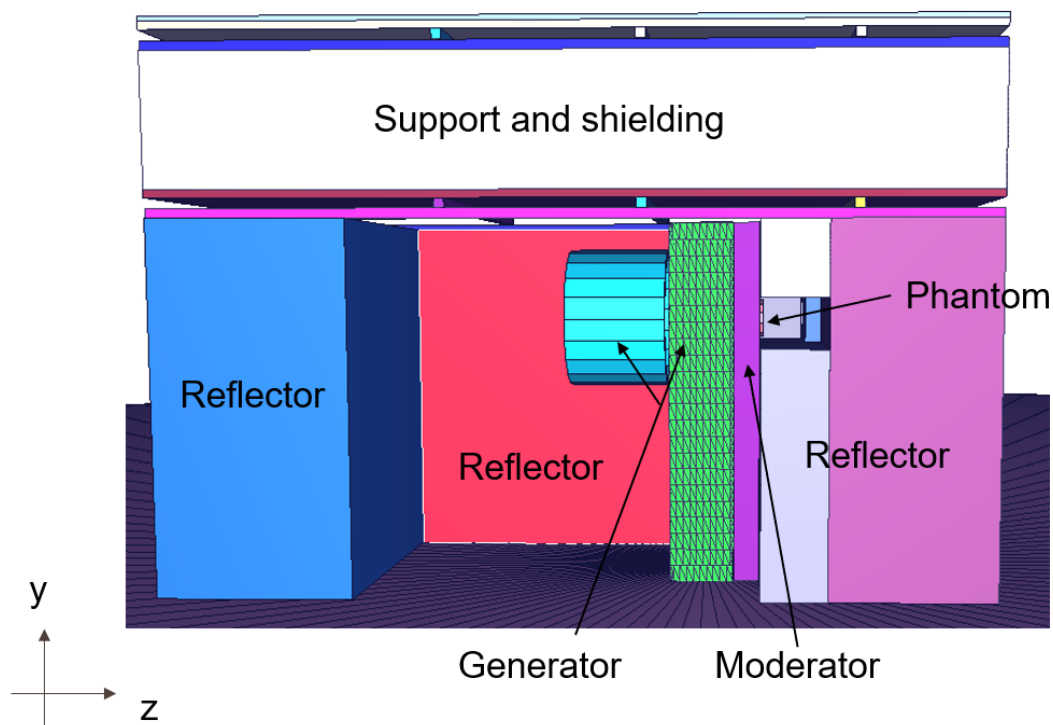


Figure 2.6 Neutron generator assembly in MCNP visualized with Visual Editor

Air fills the cavity between the blue object on the left and the neutron generator in green. For comparison, figure 2.7 depicts the neutron generator with shielding. The phantoms were simulated in the same position as the experiment and were lined up in the center of the neutron generator.



Figure 2.7 HDPE surrounds the neutron generator. The cave marked by the black arrow indicates where the phantom is placed.

### 2.3.1.2 Choice of moderator

The first simulations involving magnesium activation used only HDPE as the moderator as that reflects the actual experimental setup. However, other materials were pursued for moderating the neutrons like paraffin, heavy water, light water, and some other compounds. When simulations were done using the other materials, only the material card was changed while keeping the thickness the same. In figures 2.8 and 2.9, activated magnesium per source neutron was plotted against the energy to find which material gave the highest activation.

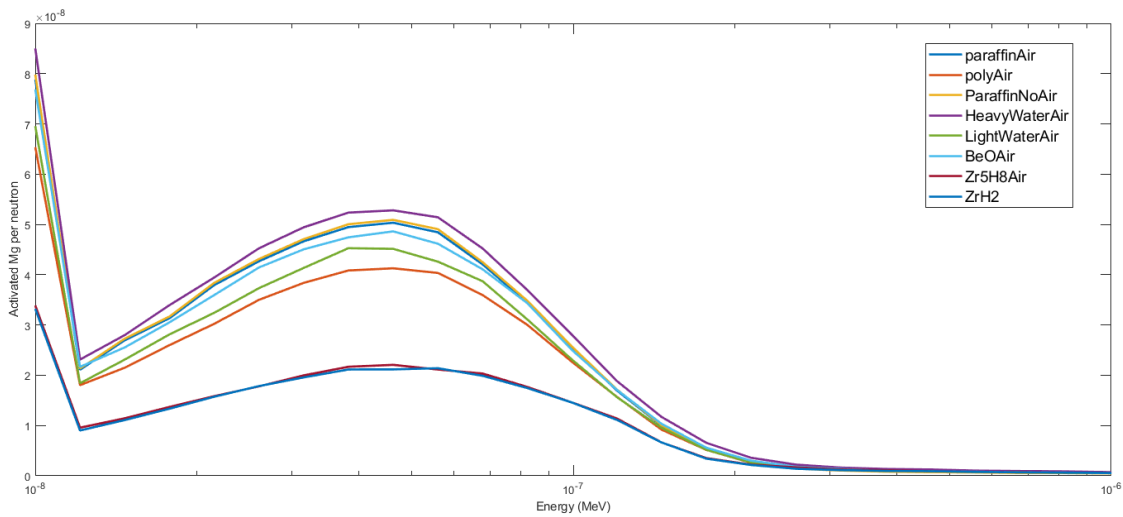


Figure 2.8 Comparing the activation of magnesium for different moderators

From figure 2.8, the legend indicated a material followed by “Air” or “NoAir” which describes if material was placed in the cavity depicted in figure 2.6. The results indicate heavy water is the best material when only considering the simulated activation of magnesium. There would be some obstacles to overcome when using heavy water as a moderator as it would limit the mobility of the neutron generator and the radiation dose should also be considered when activating an element because the goal is to have the maximum dose of 50 mSv.

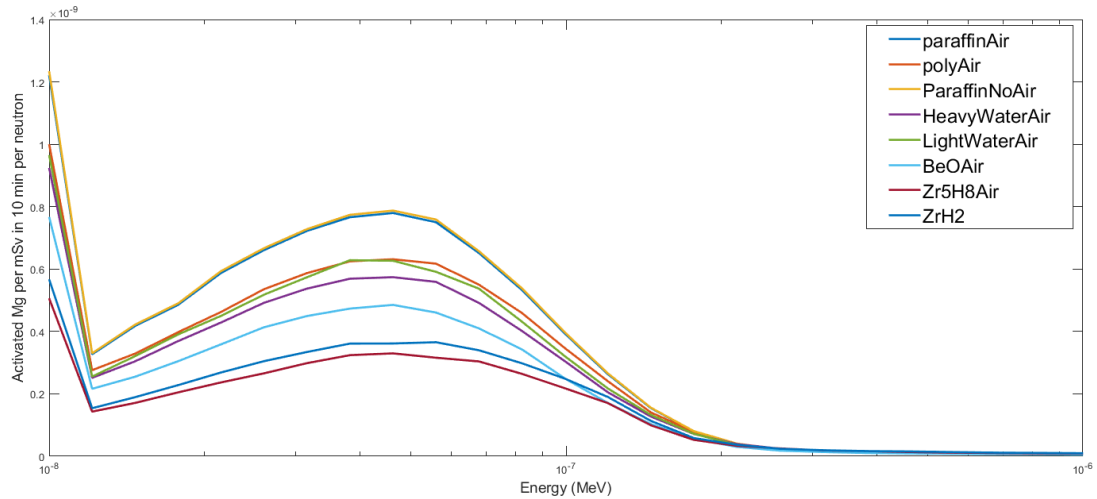


Figure 2.9 Comparing the activation of magnesium normalized to the dose in 10 minutes

Once the activated magnesium is normalized to the dose, there is a clear reduction for heavy water. Paraffin performs the best of all materials and it does not make a difference if the cavity is filled with air or paraffin based on these simulations. There is a noticeable difference between paraffin and HDPE which is currently used for experiments. The paraffin moderator performs 23% better compared to HDPE when normalizing the simulated activation of magnesium to the dose.

### 2.3.1.3 Magnesium bone doped phantom simulation

The material cards were constructed based on the phantom recipe. An example is provided in table 2.2 for the 10,000 ppm phantom.

Table 2.2 Material Card for the 10,000 ppm Magnesium Phantom

		Mg	Ca	Cl	Na	Total Mass			
	Amount from phantom, g	3.070435	57.20066	0.261938	1.466969	62			
Elements from recipe	Ca	Mg	S	O	N	H	Cl	Na	Totals
Target Mass, g	13.31572214	0.620026	11.46964	34.35539	0.310605	1.359357	0.1736	0.395666	62
MCNP input	-0.214770	-0.010000	-0.184994	-0.554119	-0.005010	-0.021925	-0.002800	-0.006382	-1



It is possible to just construct one material card and then assume the output value can be related to the other phantom concentrations using a linear relationship. In this work, a material card was constructed for each concentration to obtain outputs that were entirely dependent on the simulation. The net counts from each concentration are calculated using equation 6.

#### ***2.3.1.4 Simulated calibration line***

The net counts for magnesium were normalized to the calcium counts and then plotted against the concentration of each phantom to obtain a calibration line. The simulated calibration shown in figure 2.10 serves as comparison to the experimental calibration curve discussed in the next chapter. The purpose of having a calibration curve allows the concentration to be calculated from the net counts of a sample.

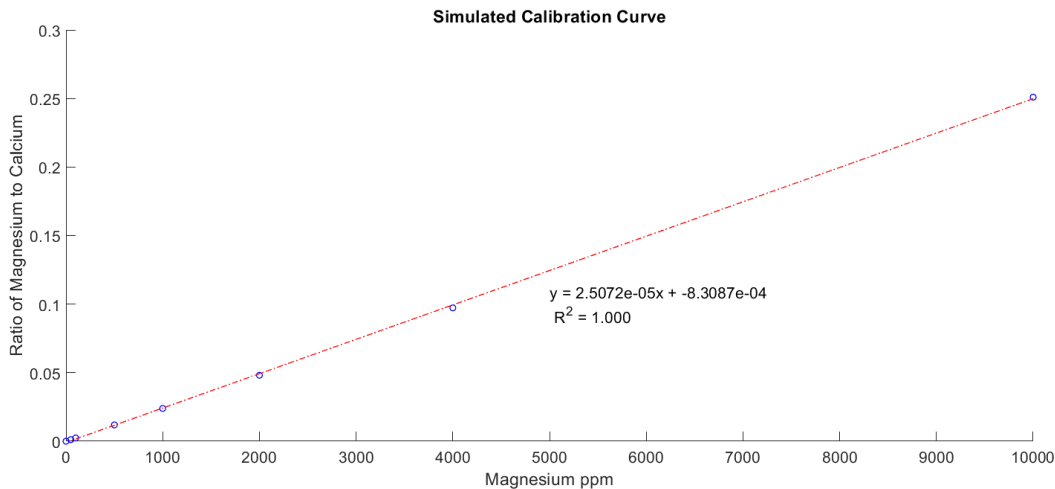


Figure 2.10 Simulated Calibration Curve

### **2.3.2 HPGc Results**

#### ***2.3.2.1 Comparing known Multi-nuclide results and simulation results***

One of the components in equation 6 is the efficiency, so the HPGc detector shown in figure 2.5 was modeled in MCNP. The source definition was calculated from the multi-nuclide

source in our lab purchased from Eckert & Ziegler. The source definition was defined by calculating the gammas per second of each nucleotide and dividing it by the total activity of the source on the day the measurement was taken.

Table 2.3 Activities of the Multi-Nuclide Source on the Day of Measurement

	Current Activity (Bq)	Current Bq/g	Gammas/s per g	gammas\s	MCNP input	Fractional amount
Cd-109	2296.039	443.794	16.110	83.346	4.150E-03	4.991E-03
Co-57	9.080	1.755	1.502	7.772	3.870E-04	4.654E-04
Te-123m *	1.324E-02	2.559E-03	2.149E-03	1.112E-02	5.536E-07	6.658E-07
Cr-51 *	5.043E-19	9.747E-20	9.610E-21	4.972E-20	2.476E-24	2.977E-24
Sn-113 *	2.714E-02	5.246E-03	3.405E-03	1.762E-02	8.771E-07	1.055E-06
Sr-85 *	1.700E-06	3.286E-07	3.234E-07	1.673E-06	8.330E-11	1.002E-10
Cs-137	7794.481	1506.570	1282.091	6633.104	3.303E-01	3.972E-01
Y-88 *	1.996E-02	3.857E-03	3.626E-03	1.876E-02	9.341E-07	1.123E-06
Co-60	4992.187	964.924	963.573	4985.198	2.482E-01	2.985E-01
Co-60	4992.187	964.924	964.731	4991.188	2.485E-01	2.989E-01
Y-88 *	1.996E-02	3.857E-03	3.834E-03	1.984E-02	9.877E-07	1.188E-06

The multi-nuclide came with a specification sheet and this information was input into an Excel spreadsheet. This allowed for an easy calculation of the current activity of the radionuclides which is needed whenever the multi-nuclide source is used. Table 2.3 displays the current activity of each radionuclide in the multi-nuclide that was used on the measurement day. It also displays the corresponding MCNP source definition. The isotopes marked with the

asterisks in table 2.3 were not included into the MCNP input because they were not present in the experimental spectrum due to their shorter half-lives. To generate the simulated spectrum, the Gaussian energy broadening (GEB) modifier was used on the f8 tally in MCNP. Figure 2.11 displays the relationship between the experimental and simulated spectrum with GEB. The simulated spectrum is slightly larger than the experimental spectrum which could be due to the simulation only considering photons.

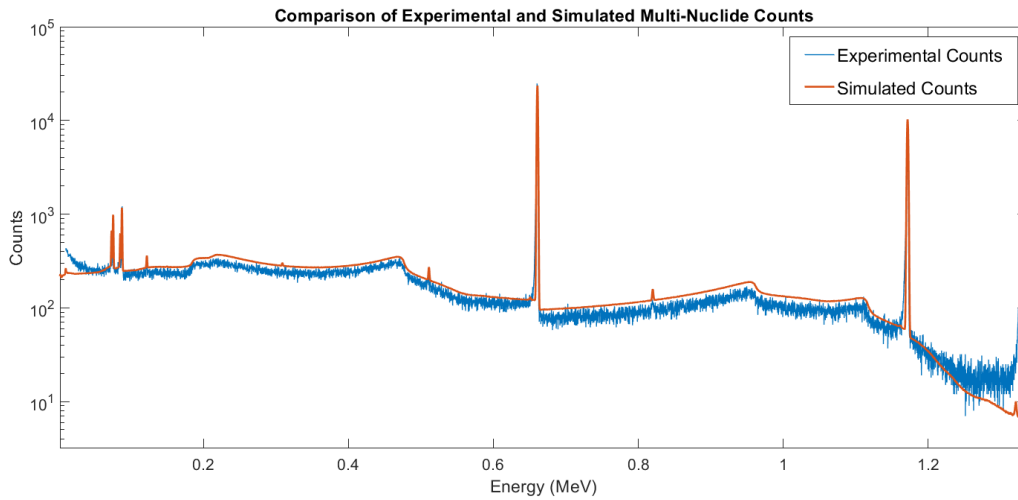


Figure 2.11 Comparing an Experimental and Simulated Multi-Nuclide Source.

GEB requires three numbers after its initiation which must be calculated from the following equations.

$$FWHM = a + b\sqrt{E + cE^2} \quad (14)$$

$$GEB \ a \ b \ c \quad (15)$$

The coefficients a, b, and c are obtained by plotting the full width half max (FWHM) of the peaks in the multi-nuclide versus the energy. Then those data points are fitted to find the coefficients.

### 2.3.2.2 Different HPGe iterations

One of the common issues in simulating HPGe detectors is in evaluating the relationship between the dead layer thickness and the efficiency [44-46]. The active volume of germanium and inactive volume of the dead layers around the active volume impact photon transmission and it was found that the manufacture's specifications needed to be slightly changed to match the experimental efficiency of the multi-nuclide source. A variety of simulations were completed to match the experimental values and this was done by increasing the thickness of the inactive layer in 1 mm increments. Figure 2.12 shows the simulation effort that went into evaluating the efficiency and energy relationship by changing the thickness of the dead layer in the simulation. Finding a suitable geometry which provides a comparable efficiency to the experiment is important because the phantom geometry needs to replace the multi-nuclide source in the simulation since there is not a standard source with the phantom's geometry.

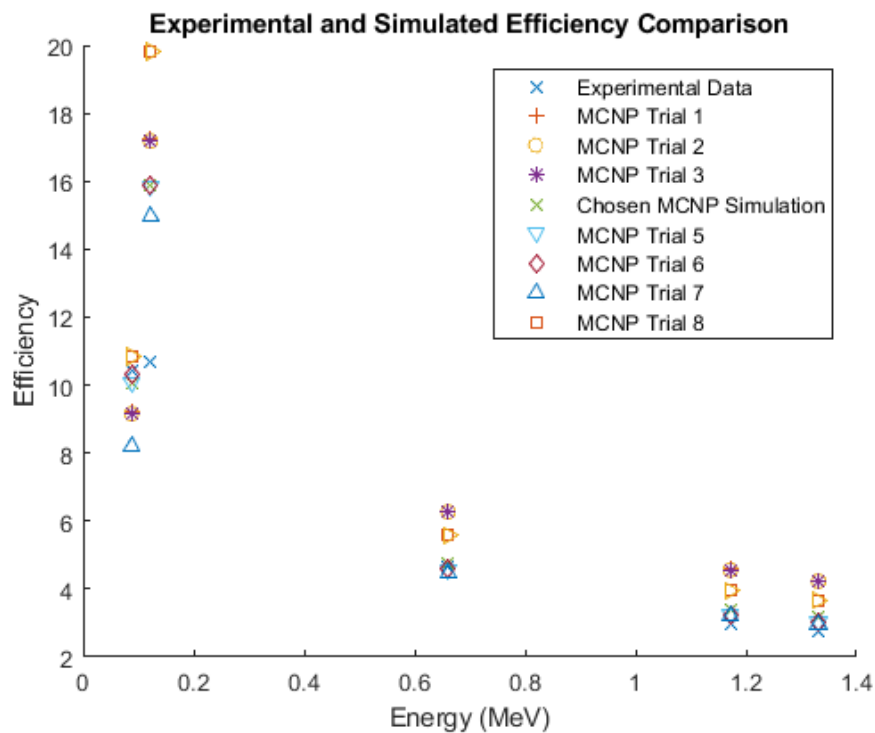


Figure 2.12 MCNP Efficiency Trials for the HPGe detector

One of the notable details from figure 2.12 is at the second lowest energy value where there is a large discrepancy between the experimental and simulated values. The reason for this difference has not been identified. In this work, 844 keV is the energy of interest and from figure 2.12, there is good agreement with the chosen simulation file at this energy. The efficiency from MCNP was calculated by taking the output value without using the GEB option and dividing it by the fractional amount of the specific isotope from the multi-nuclide source.

The purpose of making this comparison and adjusting the dead layer to obtain a similar efficiency to the experimental values is to eventually change the geometry of the multi-nuclide source to the geometry of the phantom used in the neutron activation analysis.

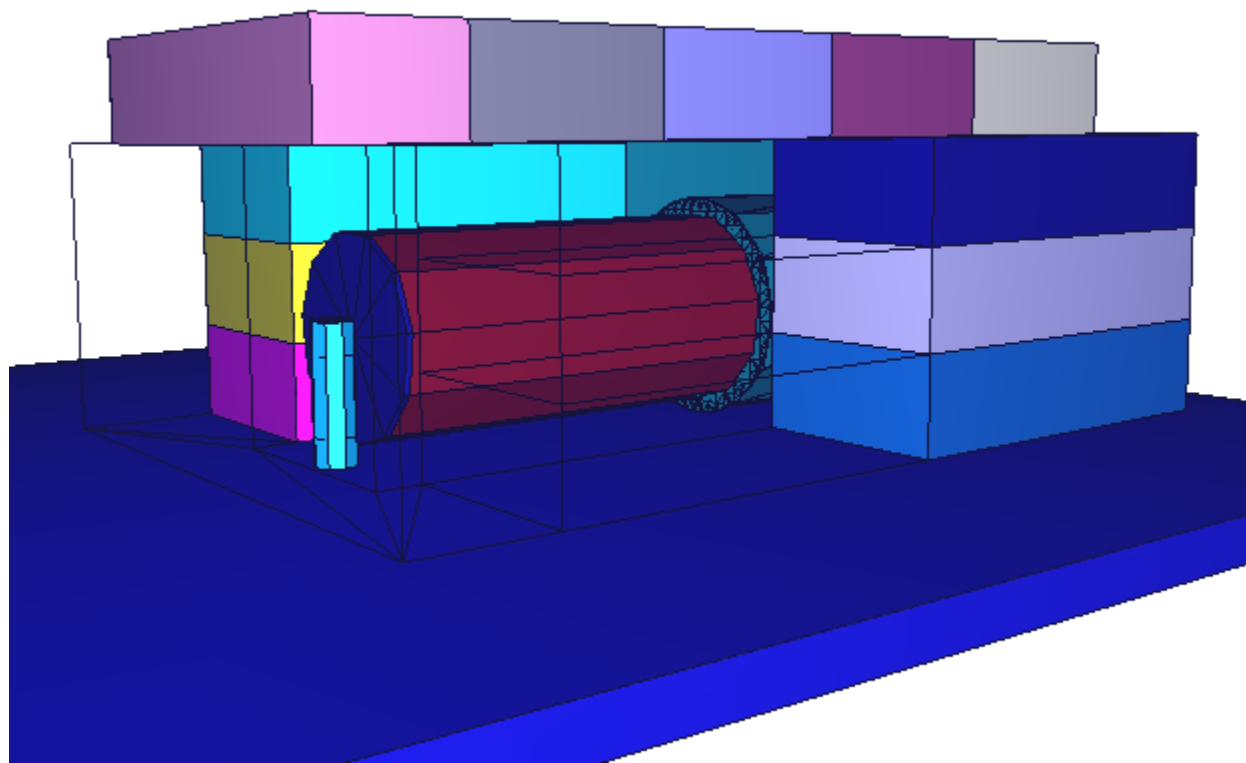


Figure 2.13 HPGe Simulation Environment with a Multi-Nuclide Source

In figure 2.13, the blocks surrounding the HPGe detector are lead and some of the bricks were selected to be wireframe to illustrate the HPGe detector and multi-nuclide source. The blue platform that everything rests on is wood. Individual lead bricks were created in MCNP to reflect the experimental setup, but this detail is not essential. A single cell could have been created to surround the HPGe detector in the simulation. A v-shaped source definition was created in MCNP to represent the multi-nuclide source from the experiment because it had a distinct v-shape at the bottom of the container. This is shown in figure 2.14.

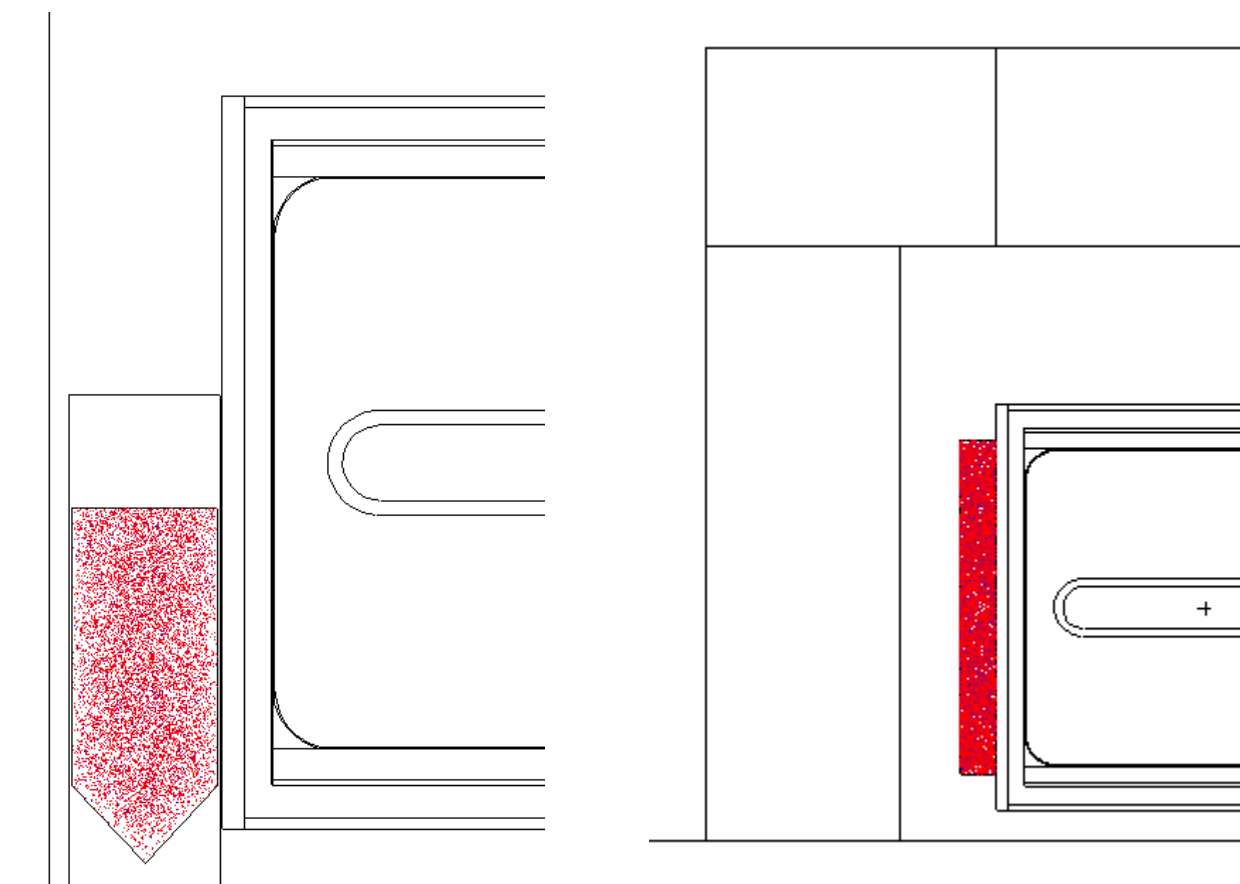


Figure 2.14 Comparing the multi-nuclide source geometry (left) and the phantom geometry (right).

In figure 2.14, the red portion represents the source particles and only a fraction of the particles is shown which is why the selected geometry is not completely red. The multi-nuclide geometry was replaced with the phantom geometry once the simulated and experimental efficiencies were comparable.

### 2.3.2.3 Efficiency Curve

An efficiency curve allows interpolation to find the efficiency at a specific energy. As discussed in the section above, the efficiency values were taken from the simulation with the phantom geometry instead of the multi-nuclide. All values had an error that was less than five percent.

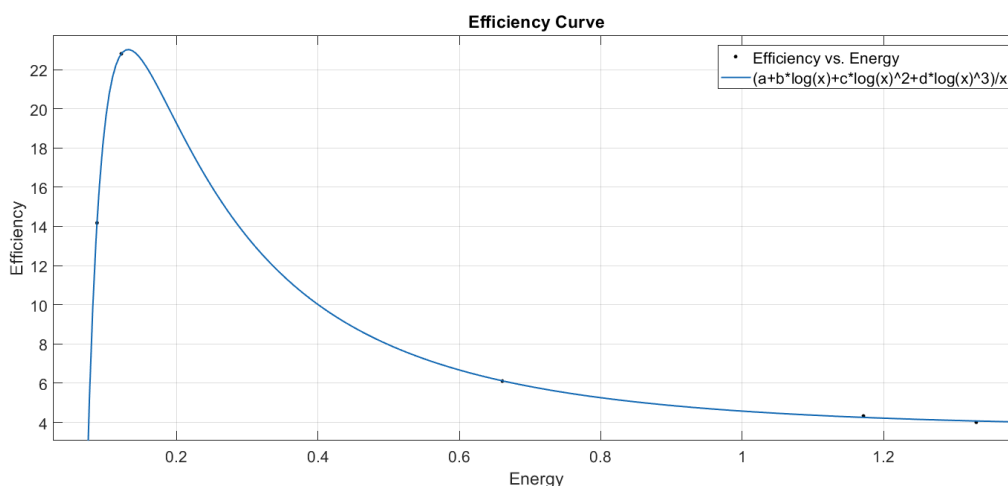


Figure 2.15 Efficiency curve used to interpolate the magnesium efficiency

An important note from figure 2.15 is that MatLab does not use the natural logarithm expression (ln), but it uses the log expression. The legend shows the equation that was used to fit the data points in figure 2.15 and this equation contains a log expression which represents the natural logarithm in MatLab. The normal representation of the base 10 logarithm is just log, but MatLab requires the user to use the term log10 instead of log to specify the difference between

the natural logarithm and a base logarithm. Another aspect that has not been discussed yet is the idea of normalization. In this work, net counts are normalized to the calcium counts to combat the irregularities of the phantom as well as attenuation that occurs within the phantom. The activated calcium energy is present at 3083 keV; however, the multi-nuclide source's highest energy was a photon from cobalt 60. The energy for calcium was still used, but the efficiency might not be as accurate. The magnesium and calcium efficiencies are displayed in table 2.4. These values are used in calculating the simulated net counts using equation 6.

Table 2.4 Magnesium and Calcium Simulated Efficiencies Based on the Phantom Geometry

Energy	Efficiency
Mg 844 keV	5.07 %
Ca 3083 keV	3.71 %

Excited magnesium also has a second gamma at 1014 keV, but this emission is not prominent and would not help in the quantification of magnesium in this work.

## 2.4 Discussion

Up to this point most of the discussion has related to simulations. These simulations lay the ground work for the experiments and serve as a means to check the experimental data to ensure its accuracy. The efficiency simulation and the moderator optimization were two components of this chapter that could be improved. In future work involving neutron activation for this system, it would be important to explore the idea of using paraffin as it has a superior activation compared to HDPE. A smaller piece of paraffin could be used as a moderator instead of replacing the entire HDPE moderator with paraffin. This approach would be a first step in



assessing paraffin's ability in activating in an element. If the experiment agrees with the simulation then the rest of the HDPE can be replaced with paraffin. The melting point of paraffin is between 58 and 62 degrees Celsius. Thus, it should maintain its structure as a moderator, but temperature measurements should be taken within the irradiation cave to confirm. The material for the reflectors in the irradiation assembly was not investigated but there are some materials that could be a competitor to high density polyethylene. Beryllium, graphite, and tungsten are common neutron reflectors; however, the cost of these items should be considered after evaluating simulation efforts. A neutron filter, not utilized in this work, could be useful in optimizing the irradiation assembly. Neutron filters help produce thermal neutrons and minimizes fast neutrons. Silicon, quartz, and sapphire have been used to filter neutrons and could be investigated to assess the impact on activation [47].

Another factor to consider when choosing paraffin as a moderator, is to consider the material card used in the simulations. The paraffin material card can be seen in appendix A and it's important to use the same material composition in the experiment as the simulation. The efficiency simulation of the HPGe are in poor agreement at the lower energies ( $<200$  keV) while there is good agreement at the higher energies. At lower energies, slight changes in the thickness of the dead layer have a larger impact compared to the higher energies. While this discrepancy doesn't impact this study, it would be prudent to explore options to obtain better agreement at the lower energies.

Recently, a member of the lab modified the source definition for the neutron simulation to include angle dependence and accounts for the experimental voltage of the neutron generator. Simulations using this source definition have not yet been explored but could make the simulation more accurate. The source definition in the neutron simulations is a point source with

a monoenergetic energy at 2.45 MeV and isn't representative of how neutrons are produced in the neutron generator.

## **CHAPTER 3. IN-VIVO QUANTIFICATION OF MANGESIUM**

### **3.1 Introduction**

The experimental portion of this work serves to validate the simulated data. This chapter will discuss the phantom construction process, the irradiation of those phantoms, and a fitting issue that arose when calculating the experimental efficiencies of the multi-nuclide source. The detection limit for this system will be calculated from the experimental data as well.

### **3.2 Materials and Methods**

#### **3.2.1 Constructing the magnesium phantom**

Magnesium doped phantoms were constructed with 4 compounds: magnesium sulfate, calcium sulfate, ammonium chloride, and sodium nitrate. As mentioned in the creating a calibration line section, the phantom recipe is in appendix B. One of the many issues that was discovered during the construction of these phantoms was exothermic reaction of magnesium sulfate and water. This reaction was prevalent once higher concentration phantoms were made beginning around 2000 ppm of magnesium.

The first iteration consisted of adding all the solid materials into a cup and then add in deionized water. Once the higher concentrations were being prepared, a noticeable exothermic reaction took place where the cup would heat up and some of the materials in the cup would quickly aggregate together. The result of this is shown in figure 3.1.

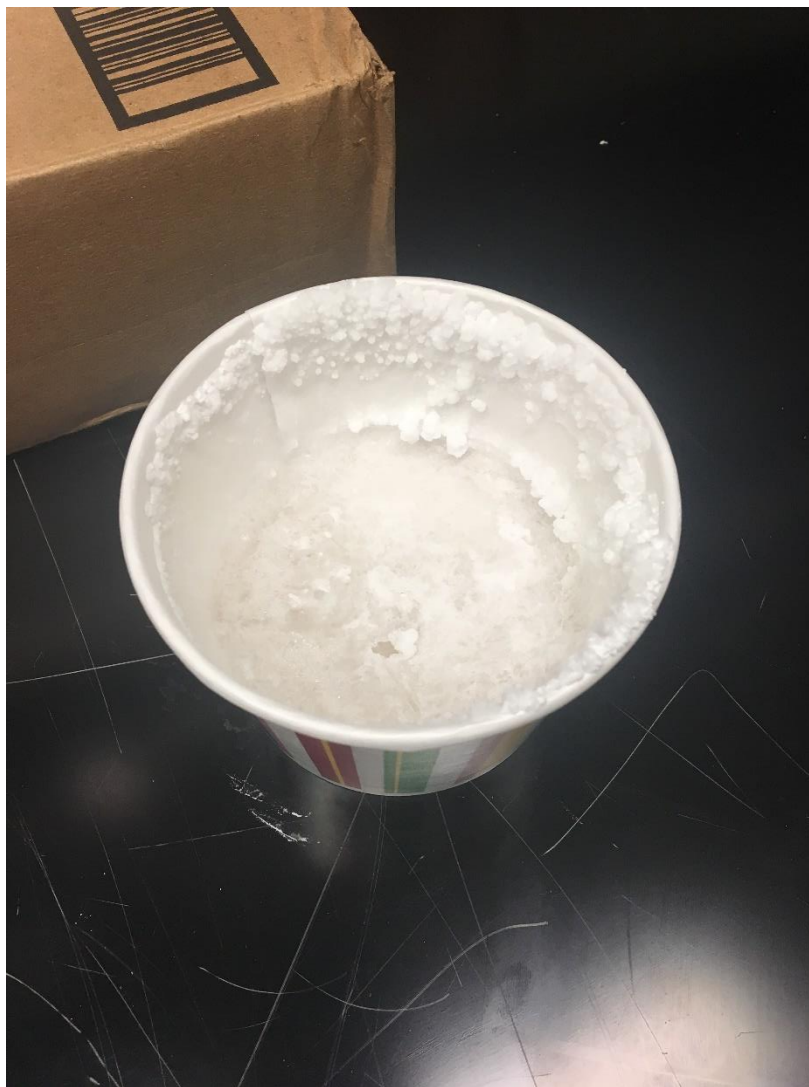


Figure 3.1 Failed magnesium phantom.

A measurement of this phantom would produce poor results from the buildup on the sides of the cup as well as being inhomogeneous. The logical next step was to only add magnesium sulfate to the cup and then add water. This solved the issues because there was no way to have a reaction between the other compounds and this avoided the aggregation. There was still an exothermic reaction, but it was more subdued. Before additional compounds were added to this cup, all the magnesium sulfate was stirred and dissolved to avoid in irregularities in the phantom.

Once dried, the phantom was removed from the cup and placed in a vacuum sealed bag which provides less interaction as opposed to the paper cup in the irradiation cave.

After solving this issue, another one appeared once the phantoms were irradiated and measured. There was manganese contamination in the phantoms, so each component was tested, and it was concluded the calcium sulfate was the culprit. This contamination is an issue because the excited gamma for manganese is at 847 keV while the excited gamma for magnesium 27 is at 844 keV. A purer calcium sulfate was ordered and tested for manganese contamination. The new compound did not show any contamination of manganese, so a new set of phantom construction began.

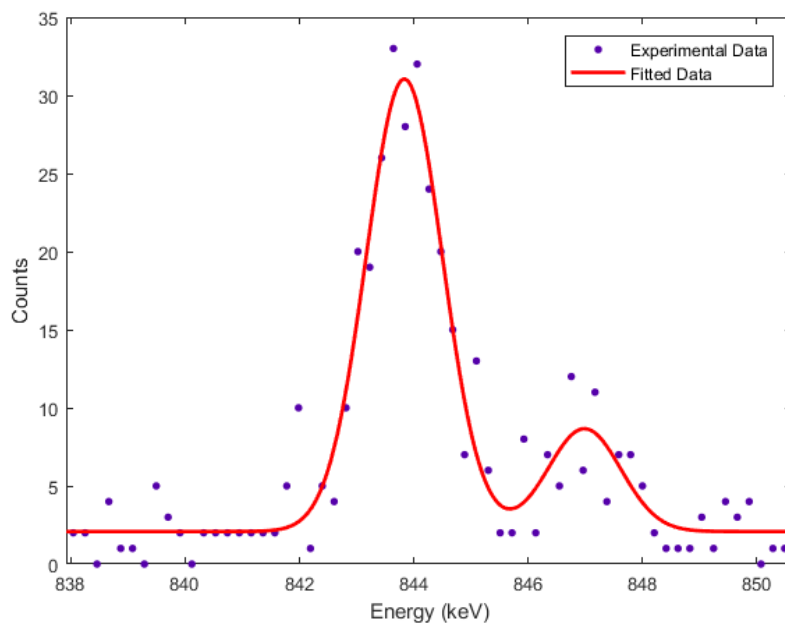


Figure 3.2 10,000 ppm phantom with old phantom recipe

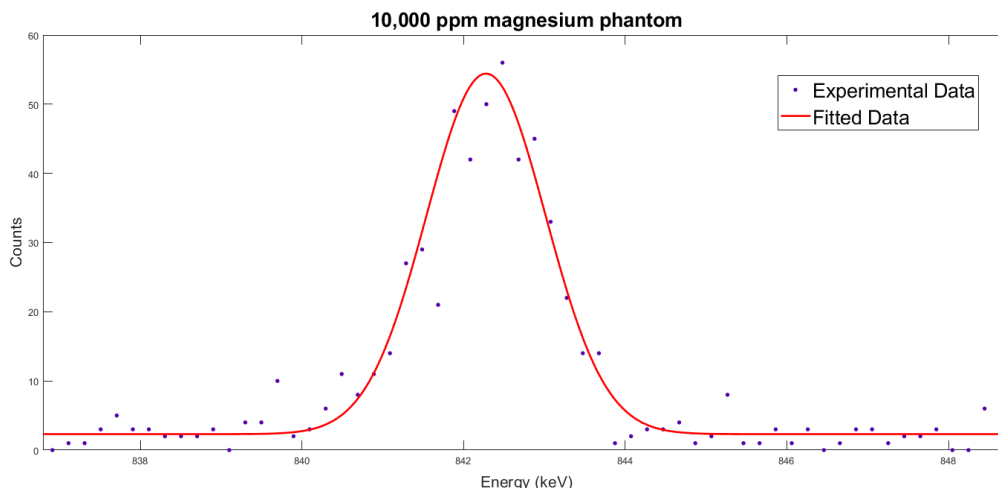


Figure 3.3 10,000 ppm phantom with new phantom recipe

Figure 3.2 and 3.3 are the result of activating magnesium 26 with thermal neutrons. The characteristic gamma ray of magnesium 27 in both graphs is at 844 keV. The spectrum was fit in MatLab to calculate the net counts, normalized to calcium, and then a calibration line can be developed when evaluating all concentrations. The same fitting algorithm was applied to each concentration. When figures 3.2 and 3.3 are compared, there are a couple aspects that are different. The first is the absence of the manganese peak in figure 3.3. The second difference is the shift in figure 3.3 compared to figure 3.2. This is a result of a different HPGe detector being used because the older one was sent for repair.

### 3.3 Results

#### 3.3.1 Fitting issue for multi-nuclide source

The multi-nuclide source previously discussed in other chapters played a role in comparing experimental and simulated efficiencies. The net counts from each isotope in the multi-nuclide are considered when calculating the efficiency.

$$\varepsilon = \frac{C}{AtI_{\gamma}} \quad (16)$$

Where C represents the net counts of the peak, A represents the total activity at the time of measurement for the isotope, t represents the counting time, and  $I_{\gamma}$  represents the abundance of the isotope. Figure 2.11 shows a comparison between the multi-nuclide source and simulation, and the two radionuclides with the strongest peaks are from cesium 137 and cobalt 60. The spectrum shows a typical looking Gaussian distribution shown in figure 3.4. On initial inspection, the fitting algorithm fits the experimental data well.

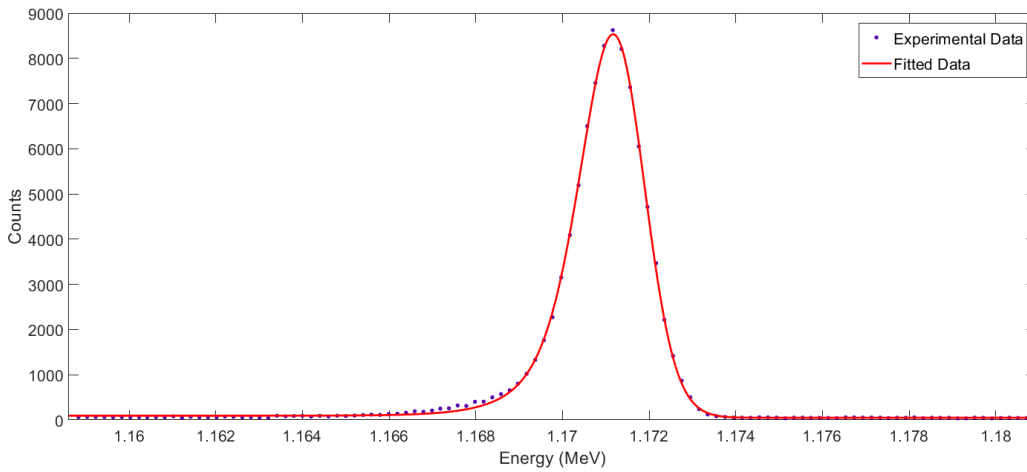


Figure 3.4 1173 keV photon of Co60 from the standard multi-nuclide source.

However, closer inspection shows a substantial lower energy tail when the y axis is in a log format. This issue was discovered when calculating the efficiency for cesium 137 and cobalt 60. The efficiency was lower than what was expected for the photons being emitted from these radionuclides. The elongated lower energy tail could be caused by a couple of factors. One factor is the activity of the source. If the source is too strong and placed very close to the detector then there is a chance to have pileup which changes the resolution of the peak. Another factor is from the insufficient collection of charges produced by the gamma rays. This phenomenon is present

in all HPGe detectors and is more apparent for larger detectors. The typical Gaussian equation needs to be modified in this case to fit the lower energy tail.

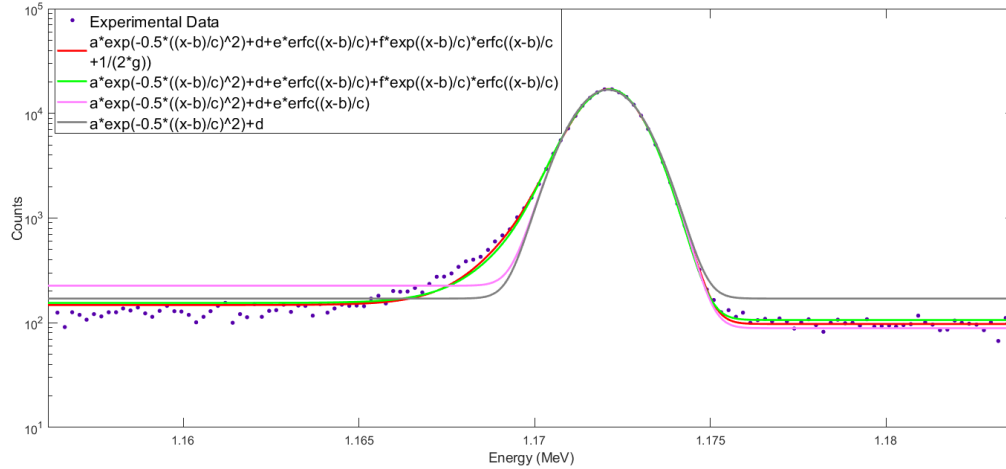


Figure 3.5 Trying different function to fit the lower energy tail

The equations used in figure 3.5 were inspired by Jin et al [43].

### 3.3.2 Phantom Results

Eight magnesium doped phantoms were created, irradiated, and then measured in the cave shown in figure 2.6. The phantoms were irradiated for 10 minutes, allowed to decay for 2 minutes, and counted for two 15 minute intervals. The first 15 minute interval was used to quantify the magnesium in the phantom. A custom script was created to eliminate the need for a person to stop the measurement, save the measurement, and then start the next measurement in Maestro. The lead sheading around the HPGe detector serves to reduce background radiation and is wrapped with tape to prevent lead contamination. Figure 3.3 represents a spectrum from the highest phantom concentration. Figure 3.6 displays the full spectrum of an activated 10,000 ppm magnesium doped phantom.



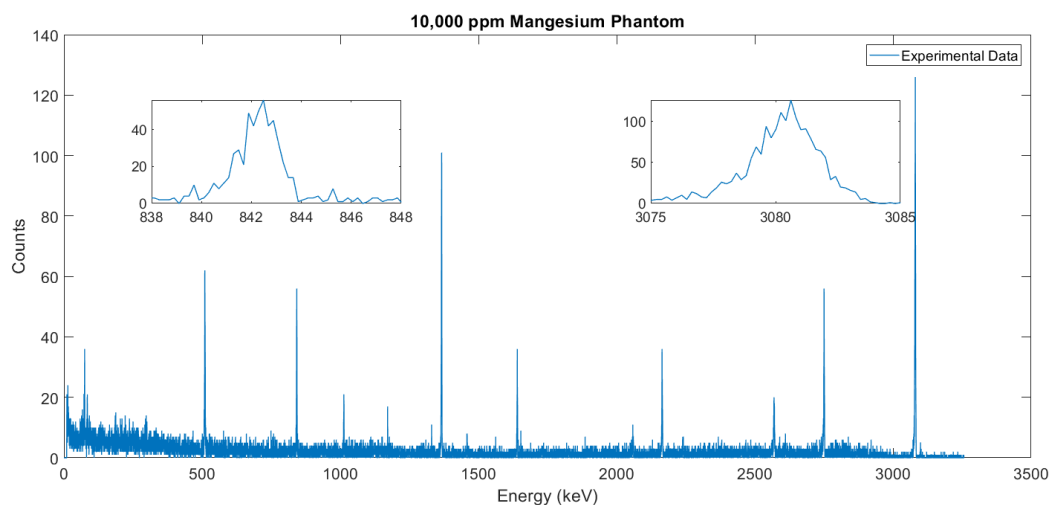


Figure 3.6 Spectrum of an activated 10,000 ppm magnesium doped phantom with the magnesium and calcium peaks in the smaller boxes.

Table 3.1 provides the net counts of magnesium and calcium from each phantom fitted in MatLab. As alluded to in earlier sections, the net counts in the table below are used to create a linear relationship between the net counts and concentration. The slope of this line is used to calculate the detection limit for the system.

Table 3.5 Net Counts from the Phantom Irradiations

Concentration (ppm)	Mg 844 keV Net Counts	Ca 3083 keV Net Counts	Ratio of Mg/Ca
10,000	483.88 ± 23.04	1716.15 ± 41.82	2.82e-1 ± 1.51e-2
4,000	167.46 ± 15.30	1849.90 ± 42.88	9.05e-2 ± 8.53e-3
2,000	96.10 ± 12.81	1962.37 ± 44.58	4.90e-2 ± 6.62e-3
1,000	45.93 ± 9.90	1852.07 ± 42.72	2.48e-2 ± 5.38e-3
500	19.44 ± 8.43	1758.64 ± 42.56	1.11e-2 ± 4.80e-3
100	10.95 ± 7.55	2013.32 ± 44.46	5.44e-3 ± 3.75e-3
50	5.50 ± 7.14	1889.80 ± 43.58	2.91e-3 ± 3.78e-3
0	3.71 ± 7.14	1547.25 ± 39.32	2.40e-3 ± 4.62e-3

The error for the net counts of magnesium and calcium were calculated by summing the array that was used to calculate the net counts and then taking the square root of that value. The error calculation for the ratio of net counts is slightly more complicated and requires the individual errors from the net counts of magnesium and calcium.

$$\sigma_{ratio} = \frac{Net\ Counts_{Mg}}{Net\ Counts_{Ca}} \sqrt{\left(\frac{\sigma_{Mg}}{Net\ Counts_{Mg}}\right)^2 + \left(\frac{\sigma_{Ca}}{Net\ Counts_{Ca}}\right)^2} \quad (17)$$

### 3.3.3 Calibration Curve

A calibration curve is a relationship between the counts of a sample and the concentration of a sample. Two calibration curves were developed from the data in table 3.1 where the counts or ratio of the counts are plotted against the phantom concentration. A linear relationship can be

fit to these data points to establish a means to find the minimum detection level of the current irradiation assembly.

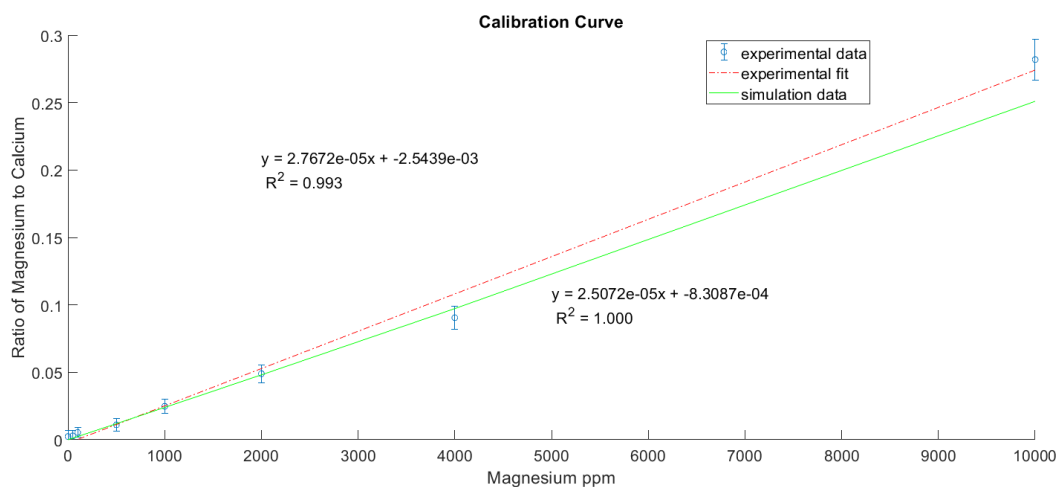


Figure 3.7 Comparing the simulated and experimental calibration curves

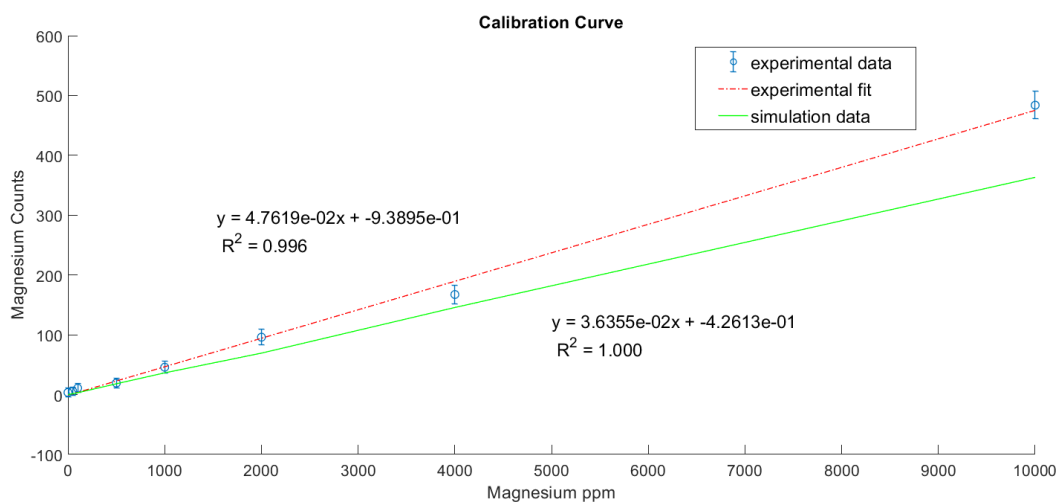


Figure 3.8 Comparing the simulated and experimental calibration curves without normalizing to calcium.

These calibration curves allow the concentration of magnesium to be calculated from a sample and detection limit can be calculated from the slope in these graphs. The percent difference of the slopes offer an indication into the similarity between the experimental and

simulation. The percent difference when normalizing to calcium is equal to 9.40% and when the magnesium counts are not normalized to calcium, the percent difference is equal to 23.66%. This calculation reiterates the importance of normalization to correct for inhomogeneities.

### 3.3.4 Detection Limit

The detection limit is defined as the minimum concentration that can be detected above background. As alluded to in the previous section, the detection limit calculation utilizes the slope from the calibration line.

$$DL = \frac{2\sigma_{0\text{ ppm}}}{m} \quad (18)$$

Where  $\sigma_{0\text{ ppm}}$  represents the error in the ratio of the magnesium and calcium counts at 0 ppm and  $m$  represents the slope from the experimental calibration line. The variable  $\sigma_{0\text{ ppm}}$  is calculated using equation 17 where the 0 ppm net counts are used for magnesium and calcium. Table 3.2 presents the detection limit for magnesium in this neutron activation system.

Table 3.6 The calculated Detection Limit of Magnesium for the Neutron Generator in this Work

	Normalizing to calcium	No normalization
Detection Limit	334 ppm	300 ppm

### 3.3.5 Dose

An electronic dosimeter was placed in the irradiation cave next to the phantoms and recorded the gamma and neutron dose. Both doses were recorded after the irradiation was complete. The skin has a radiation weighting factor of 0.01 [48] and to calculate the whole body dose the dose to the hand needs to correlate to the mass of the body. The mass of the hand can

vary depending on age and gender. A middle aged man has a hand mass equal to 525 grams and the total body weight is 70,000 grams, so the mass of the hand accounts for 0.7% percent of the total body weight [49].

The average dose from neutrons and photons for the phantom irradiations was 1.69 rem and 428.70 mrem, respectively. The whole body dose for the 10 minutes is calculated using equation 19.

$$D = 9.3 \mu Sv + 0.01 * 0.007 * \left( \frac{1.69}{100} * 1e6 + \frac{0.4287}{100} * 1e6 \right) = 10.79 \mu Sv \quad (19)$$

$$\cong 11 \mu Sv$$

The average dose across the irradiations was converted to Sieverts and then to micro Sieverts. This quantity was multiplied by the tissue weighting factor for bone and the mass percent of the hand relative to the whole body.  $9.3 \mu Sv$  accounts for the background radiation measured in the laboratory in 10 minutes.

### 3.3.6 Discussion

The simulated and experimental calibrations difference can be attributed to a couple of factors. The simulation is dependent on the efficiency simulation of the multi-nuclide and being able to match the efficiency values. While there was close agreement with the higher energies, extrapolation was needed to calculate the efficiency of calcium since the lab does not have a radionuclide that approaches 3 MeV. Extrapolation of the calcium efficiency gave a reasonable value, but it may not be completely correct. In constructing the phantoms, there is always a possibility of human error being introduced when measuring the material.

The HPGe in this work was sufficiently far away from the neutron generator and it is not expected that neutrons could damage the detector. However, if the HPGe detector is close to the

neutron generator (i.e. associated particle imaging) then a lower energy tail can develop. Neutron damage has the capability of creating an elongated lower energy tail by preventing charge carriers from reaching the electrodes [50].

A total whole body of  $11 \mu Sv$  was determined as the average dose a subject would receive for a measurement. This dose is comparable to a chest PA radiograph of  $20 \mu Sv$  [51]. Equation 19 is somewhat of a pseudo calculation of dose because it isn't common to use the mass percentage of a body part to calculate the whole body dose; however, it's logical to use that approach in this work because the hand would primarily be subject to the dose in the irradiation cave.

One limitation of this work has not been discussed yet. In the experiment and simulation, the phantom was a bone like material without tissue being present. According to ICRP 23, there is 5.3 grams of magnesium in skeletal muscle which is equivalent to approximately 200 ppm of magnesium in muscle. Considering the range of magnesium in bone, the ratio of magnesium in muscle to bone is less than 10 percent. To better understand the contribution of skeletal muscle and tissue, simulations could be done which have skeletal muscle and tissue on the phantom. Furthermore, phantoms can be constructed which contain a tissue equivalent or muscle equivalent on the magnesium phantoms.

## CHAPTER 4. CONCLUSION

The first part of this work focused on the simulation of HPGe detector and neutron generator. The HPGe simulation had good agreement at the higher energies which was important because the excited energy of magnesium 27 is 844 keV. Although there was poor agreement at the lower energies, it was decided that the higher energy values were comparable to the experiment. The geometry of the neutron generator simulation was modeled with the same dimensions of the actual generator in the laboratory. The source definition in the simulation was a monoenergetic point source which is not representative of the neutrons that produced in the generator; however, there is a newly developed source bias that has not been tested on the activation of magnesium. This bias accounts for angular distribution and the voltage the neutron generator is run during an experiment. Including this bias in the simulation may improve the accuracy of the neutron simulation.

The *in-vivo* study for the magnesium doped phantoms correlated well with the simulated study. The whole body dose for the experiment was comparable to a chest PA radiograph suggesting that the dose is acceptable. While this is the case, the dose should always be reduced permitting the outcome of the experiment maintains its integrity. The normalized detection limit of 334  $\mu\text{g}$  magnesium per gram of cortical bone is much less than the range of magnesium concentration found in cortical bone, which is about 2625-3500 ppm [1-3]. The detection limit from the phantom study suggests it should be able to quantify the amount of magnesium in a human subject.

There is no current technique to assess magnesium storage in human body. The techniques that currently measure magnesium rely on a biomarker which accounts for less than one percent of magnesium stored in the body. IVNAA is a promising technology to quantify the

magnesium content of the body. It can be used to study health effects that are related to magnesium insufficiency or overtake. The sensitivity of the system can be improved with some modifications of the current system, and the system will eventually be used to quantify multiple essential elements for the body, including magnesium.



## REFERENCES

- [1] Glasdam, S. M., Glasdam, S., & Peters, G. (2016). The Importance of Magnesium in the Human Body: A Systematic Literature Review. *Advan. Clin. Chem.*, 73, 169-193. doi:10.1016/bs.acc.2015.10.002
- [2] Elin, R. J. (1987). Assessment of magnesium status. *Clinical Chemistry*, 33(11), 1965-1970.
- [3] Richmond, C. R. (1986). ICRP publication 23. *International Journal of Radiation Oncology, Biology, Physics*, 12(3), 433-433. doi:10.1016/0360-3016(86)90366-4
- [4] Elin, R. J. (1994). Magnesium: the fifth but forgotten electrolyte. *American journal of clinical pathology*, 102(5), 616. doi:10.1093/ajcp/102.5.616
- [5] Institute of Medicine . Standing Committee on the Scientific Evaluation of Dietary Reference, I. (1997). *Dietary reference intakes : for calcium, phosphorus, magnesium, vitamin D, and fluoride*. Washington, D.C.: Washington, D.C. : National Academy Press.
- [6] de Baaij, J., Hoenderop, J., & Bindels, R. (2015). Magnesium in Man: Implications for Health and Disease. *Physiological Reviews*, 95(1), 1. doi:10.1152/physrev.00012.2014
- [7] Derouffignac, C., & Quamme, G. (1994). RENAL MAGNESIUM HANDLING AND ITS HORMONAL-CONTROL. *Physiol. Rev.*, 74(2), 305-322. doi:10.1152/physrev.1994.74.2.305
- [8] Swaminathan, R. (2003). Magnesium metabolism and its disorders. *The Clinical biochemist. Reviews*, 24(2), 47.
- [9] Moshfegh A Goldman JD Ahuja J, et al. What We Eat in America, NHANES 2005–2006: Usual Nutrient Intakes from Food and Water Compared to 1997 Dietary Reference Intakes for Vitamin D, Calcium, Phosphorus, and Magnesium. Available at: [http://www.ars.usda.gov/SP2UserFiles/Place/12355000/pdf/0506/usual\\_nutrient\\_intake\\_vitD\\_ca\\_phos\\_mg\\_2005-06.pdf](http://www.ars.usda.gov/SP2UserFiles/Place/12355000/pdf/0506/usual_nutrient_intake_vitD_ca_phos_mg_2005-06.pdf). Accessed 27 May 2019.
- [10] Landi, E., Tampieri, A., Mattioli-Belmonte, M., Celotti, G., Sandri, M., Gigante, A., . . . Biagini, G. (2006). Biomimetic Mg- and Mg,CO 3-substituted hydroxyapatites: synthesis characterization and in vitro behaviour. *Journal of the European Ceramic Society*, 26(13), 2593-2601. doi:10.1016/j.jeurceramsoc.2005.06.040
- [11] Rude, R. K., & Gruber, H. E. (2004). Magnesium deficiency and osteoporosis: animal and human observations. *The Journal of Nutritional Biochemistry*, 15(12), 710-716. doi:10.1016/j.jnutbio.2004.08.001
- [12] Jahnen-Dechent, W., & Ketteler, M. (2012). Magnesium basics. *Clin Kidney J*, 5(Suppl 1), i3-i14. doi:10.1093/ndtplus/sfr163

- [13] Arsenian, M. A. (1993). Magnesium and cardiovascular disease. *Progress in Cardiovascular Diseases*, 35(4), 271-310. doi:10.1016/0033-0620(93)90008-2
- [14] Pham, P., Pham, P., Pham, S. V., Miller, J., & Pham, P. (2007). Hypomagnesemia in patients with type 2 diabetes. *Clin. J. Am. Soc. Nephrol.*, 2(2), 366-373. doi:10.2215/CJN.02960906
- [15] Song, Y., He, K., Levitan, E. B., Manson, J. E., & Liu, S. (2006). Effects of oral magnesium supplementation on glycaemic control in Type 2 diabetes: a meta- analysis of randomized double- blind controlled trials. In (Vol. 23, pp. 1050-1056). Oxford, UK.
- [16] Sojka, J. E., & Weaver, C. M. (1995). Magnesium supplementation and osteoporosis. *Magnesium supplementation and osteoporosis*(3), 71-74.
- [17] Onishi, S., & Yoshino, S. (2006). Cathartic-induced fatal hypermagnesemia in the elderly. *Internal medicine (Tokyo, Japan)*, 45(4), 207. doi:10.2169/internalmedicine.45.1482
- [18] Elin, R. J. (1988). Magnesium metabolism in health and disease. *Disease-a-Month*, 34(4), 166-218. doi:10.1016/0011-5029(88)90013-2
- [19] Cholest, I. N., Steinberg, S. F., Tropper, P. J., Fox, H. E., Segre, G. V., & Bilezikian, J. P. (1984). The influence of hypermagnesemia on serum calcium and parathyroid hormone levels in human subjects. *The New England journal of medicine*, 310(19), 1221. doi:10.1056/NEJM198405103101904
- [20] Iseri, L. T., & French, J. H. (1984). Magnesium: Nature's physiologic calcium blocker. *American Heart Journal*, 108(1), 188-193. doi:10.1016/0002-8703(84)90572-6
- [21] Elin, R. J. (2010). Assessment of magnesium status for diagnosis and therapy. *Magnesium Research*, 23(4), S194-S198. doi:10.1684/mrh.2010.0213
- [22] Yu, L., Davis, W., Nuevo Ordonez, Y., & Long, S. (2013). Fast and accurate determination of K, Ca, and Mg in human serum by sector field ICP-MS. *Analytical and Bioanalytical Chemistry*, 405(27), 8761-8768. doi:10.1007/s00216-013-7320-4
- [23] Harrington, J., Young, D., Essader, A., Sumner, S., & Levine, K. (2014). Analysis of Human Serum and Whole Blood for Mineral Content by ICP-MS and ICP-OES: Development of a Mineralomics Method. *Biological Trace Element Research*, 160(1), 132-142. doi:10.1007/s12011-014-0033-5
- [24] Piruzian, L. A., Protasova, O. V., Maksimova, I. A., Morukov, B. V., Protasov, S. V., & Ushakov, I. B. (2015). Magnesium level in the human body during a 105-day isolation.(Author abstract). 41(7), 746. doi:10.1134/S0362119715070178
- [25] Feillet-Coudray, C., Coudray, C., Gueux, E., Mazur, A., & Rayssiguier, Y. (2003). New In Vitro Blood Load Test Using a Magnesium Stable Isotope for Assessment of Magnesium Status. *New In Vitro Blood Load Test Using a Magnesium Stable Isotope for Assessment of Magnesium Status*, 133(4), 1220-1223. doi:10.1093/jn/133.4.1220

- [26] Avioli, L. V., & Berman, M. (1966). Mg<sup>28</sup> kinetics in man. *Journal of applied physiology*, 21(6), 1688. doi:10.1152/jappl.1966.21.6.1688
- [27] Laurencin, D., Almora-Barrios, N., de Leeuw, N. H., Gervais, C., Bonhomme, C., Mauri, F., . . . Smith, M. E. (2011). Magnesium incorporation into hydroxyapatite. *Biomaterials*, 32(7), 1826-1837. doi:10.1016/j.biomaterials.2010.11.017
- [28] Alfrey, A. C., & Miller, N. L. (1973). Bone magnesium pools in uremia. *The Journal of clinical investigation*, 52(12), 3019. doi:10.1172/JCI107500
- [29] Aslam, Pejović-Milić, A., McNeill, F. E., Byun, S. H., Prestwich, W. V., & Chettle, D. R. (2008). In vivo assessment of magnesium status in human body using accelerator-based neutron activation measurement of hands: a pilot study. *Med Phys*, 35(2), 608-616. doi:10.1118/1.2830383
- [30] Ryan, C., Marianno, C., Charlton, W., & James, W. (2012). Neutron activation analysis of concrete for cross-border nuclear security. *An International Journal Dealing with All Aspects and Applications of Nuclear Chemistry*, 291(1), 267-272. doi:10.1007/s10967-011-1272-y
- [31] Oak Ridge National, L., United States. Dept. of, E., & United States. Dept. of Energy. Office of Scientific and Technical, I. (1994). *Methods for preparing comparative standards and field samples for neutron activation analysis of soil*. Washington, D.C. : Oak Ridge, Tenn.: Washington, D.C. : United States. Dept. of Energy ; Oak Ridge, Tenn. : distributed by the Office of Scientific and Technical Information, U.S. Dept. of Energy.
- [32] Cotter, M. J. (1981). Neutron Activation Analysis of Paintings: Autoradiography following neutron irradiation provides information for authentication and restoration and reveals the existence of underpaintings undetected by other means. *American Scientist*, 69(1), 17-27.
- [33] Oak Ridge National, L., & United States. Dept. of Energy. Office of Scientific and Technical, I. (1981). *Radioactive decay data tables*. Oak Ridge, Tenn. : Oak Ridge, Tenn.: Oak Ridge, Tenn. : Oak Ridge National Laboratory. ; Oak Ridge, Tenn. : distributed by the Office of Scientific and Technical Information, U.S. Dept. of Energy.
- [34] Walkiewicz, T. A., Raman, S., Journey, E., Starner, J. W., & Lynn, J. (1992). THERMAL-NEUTRON CAPTURE BY MAGNESIUM ISOTOPES. *Phys. Rev. C*, 45(4), 1597-1608.
- [35] Magnesium Cross Section. (n.d.). Retrieved from <https://www-nds.iaea.org>
- [36] T. Goorley *et al* 2012 Initial MCNP6 Release Overview *Nuclear Technology* 180 298-315
- [37] Liu, Y., Rolle-Mcfarland, D., Mostafaei, F., Zhou, Y., Li, Y., Zheng, W., . . . Nie, L. H. (2018). In vivo neutron activation analysis of bone manganese in workers. *Physiological measurement*, 39(3), 035003. doi:10.1088/1361-6579/aaa749

- [38] Byrne, P., Mostafaei, F., Liu, Y., Blake, S. P., Koltick, D., & Nie, L. H. (2016). The study of in vivo quantification of aluminum (al) in human bone with a compact dd generator-based neutron activation analysis (naa) system. *Physiological Measurement*, 37(5), 649-660. doi:10.1088/0967-3334/37/5/649
- [39] Coyne, M. D., Neumann, C., Zhang, X., Byrne, P., Liu, Y., Weaver, C. M., & Nie, L. H. (2018). Compact DD generator-based in vivo neutron activation analysis (IVNAA) system to determine sodium concentrations in human bone. *Physiological Measurement*, 39(5). doi:10.1088/1361-6579/aabe66
- [40] McConn, R. J., Gesh, C. J., Pagh, R. T., Rucker, R. A., & Williams Iii, R. (2011). Compendium of Material Composition Data for Radiation Transport Modeling - PNNL-15870 Rev. 1. In: Pacific Northwest National Laboratory (PNNL), Richland, WA (US) ; Sponsoring Organization: USDOE.
- [41] PROTECTION AGAINST NEUTRON RADIATION. - NCRP--38. (1971). In: National Council on Radiation Protection and Measurements, Washington, D. C.
- [42] Richmond, C. R. (1986). ICRP publication 23. *International Journal of Radiation Oncology, Biology, Physics*, 12(3), 433-433. doi:10.1016/0360-3016(86)90366-4
- [43] Jin, Y., Gardner, R. P., & Verghese, K. (1986). A semi-empirical model for the gamma-ray response function of germanium detectors based on fundamental interaction mechanisms. *Nuclear Inst. and Methods in Physics Research, A*, 242(3), 416-426. doi:10.1016/0168-9002(86)90440-7
- [44] Chham, E., García, F. P., El Bardouni, T., Ferro-García, M. A., Azahra, M., Benaalilou, K., . . . Kaddour, M. (2015). Monte Carlo analysis of the influence of germanium dead layer thickness on the HPGe gamma detector experimental efficiency measured by use of extended sources. *Applied Radiation and Isotopes*, 95, 30-35. doi:10.1016/j.apradiso.2014.09.007
- [45] Ródenas, J., Pascual, A., Zarza, I., Serradell, V., Ortiz, J., & Ballesteros, L. (2003). Analysis of the influence of germanium dead layer on detector calibration simulation for environmental radioactive samples using the Monte Carlo method. In (Vol. 496, pp. 390-399).
- [46] Chuong, H. D., Thanh, T. T., Ngoc Trang, L. T., Nguyen, V. H., & Tao, C. V. (2016). Estimating thickness of the inner dead-layer of n-type HPGe detector. *Applied Radiation and Isotopes*, 116, 174-177. doi:10.1016/j.apradiso.2016.08.010
- [47] Stamatelatos, I. E., & Messoloras, S. (2000). Sapphire filter thickness optimization in neutron scattering instruments. *Review of Scientific Instruments*, 71(1), 70-73. doi:10.1063/1.1150163
- [48] ICRP, 2007. The 2007 Recommendations of the International Commission on Radiological Protection. ICRP Publication 103. *Ann. ICRP* 37 (2-4).

- [49] Clauser, C. E., McConville, J. T., & Young, J. W. (1969). WEIGHT, VOLUME, AND CENTER OF MASS OF SEGMENTS OF THE HUMAN BODY. In U. S. D. o. t. A. Force & O. H. Antioch Coll Yellow Springs (Eds.): Defense Technical Information Center.
  
- [50] Idaho National, L., United States. Dept. of, E., & United States. Dept. of Energy. Office of Scientific and Technical, I. (2013). Neutron Damage in Mechanically-Cooled High-Purity Germanium Detectors for Field-Portable Prompt Gamma Neutron Activation Analysis (PGNAA) Systems. Washington, D.C. : Oak Ridge, Tenn.: Washington, D.C. : United States. Dept. of Energy. ; Oak Ridge, Tenn. : distributed by the Office of Scientific and Technical Information, U.S. Dept. of Energy.
  
- [51] Bushberg, J. T. (2012). The essential physics of medical imaging (3rd ed.. ed.): Philadelphia : Wolters Kluwer Health/Lippincott Williams & Wilkins

## APPENDIX A. DETAILS OF SIMULATION AND EXPERIMENT PHANTOM CONCENTRATIONS

### NEUTRON GENERATOR INPUT FILE

MCNPX Visual Editor Version X\_24E

```

1  208 -2.699 -1 :-20 :-21 :-22 :-23 :(-24 25 )
2  204 -0.001225 1 2 3 4 5 6 7 8 9 10 11 12 13 14 15 16 17 18 19 20 21 22
    23 24 25 #16 #17 #18 #20 #21 #22 #23 #25 #26 #29 -200 #305 #306 #30
    #31 #32 #33 #34 #35 #36 #37 #38 #39 #40 #41 #42 #43 #44 #47 #48
3  256 -0.93 (-2 15 16 ):-3 :-4 :-5 :-6 :-7 15 17 18 19 #4
4  204 -0.001225 #12 #13 -8
5  204 -0.001225 200
6  208 -2.699 (-9 10 ):(-11 12 ):(-13 14 )
7   0      #3 #4 #12 #13 #14 -10
8   0      #3 #4 #13 #14 -12 :-14
10  317 -4.98 -15
11  209 -8.96 #10 -16
12  498 -4.506 -17
13  208 -2.699 -18 19
14   0      #4 #12 -19
15   0      #6 #8 -25
16  256 -0.93 26 -27 -1.1 -1.2 -45 -1.4 $d2o
17  252 -11.35 32 -33 30 -31 29 -28 $lead
18  252 -11.35 -35 34 32 -36 29 -28 $lead
c 19  256 -0.93 -28 -1.2 32 -38 37 -45 $pe
20  256 -0.93 -40 34 -45 32 -38 39
21  256 -0.93 44 -41 -1.4 32 -38 -40 27
22  256 -0.93 42 -1.4 44 -45 -40 -43
23  256 -0.93 44 -40 68 -46 47 -43
25  256 -0.93 44 37 -45 32 -42 -39 27

```

26 256 -0.93 44 -49 -1.4 -45 305 -32  
 c 27 256 -0.93 44 -50 -1.4 -51 42 -43  
 c 28 256 -0.93 44 -50 35 -31 42 -43  
 29 307 -1.85 33 -55 -54 \$phantom  
 305 256 -0.93 -305 47 -45 -1.4 44 -40  
 306 256 -0.93 20.1 305 -32 -40 -45 -21.4  
 30 492 -7.86 47 45 -43 -58 65 -64  
 31 492 -7.86 66 -67 47 45 -43 -58  
 32 492 -7.86 -63 58 56 -60 44 -40  
 33 492 -7.86 -63 58 62 -59 44 -40  
 34 492 -7.86 -63 58 61 -57 44 -40  
 35 524 -0.64 63 -68 47 -43 44 -40  
 36 492 -7.86 -48 -69 46 -43 -64 65 47  
 37 492 -7.86 -48 -69 46 -43 66 -67 47  
 38 492 -7.86 48 -69 61 -57 44 -40  
 39 492 -7.86 48 -69 62 -59 44 -40  
 40 492 -7.86 48 -69 56 -60 44 -40  
 41 524 -0.64 69 -71 -70 47 -40 -43 44  
 42 252 -11.35 70 -71 47 -40 -43 44  
 43 468 -1.406 73 21.4 -200  
 44 228 -2.35 -73 -200  
 c 45 256 -0.93 305 49 -20.1 24.6 -21.4 -45 (13.3 :9.1 )#6 #8 #15 \$filler  
 c 46 256 -0.93 47 -43 45 -63 44 -40 #32 #33 #34 #30 #31 \$filler  
 47 256 -0.93 41 -37 32 -38 44 1.2 \$block opening to cave  
 48 256 -0.93 36 -42 34 -37 -39 29 -28  
  
 c Aluminum cover - face  
 1 rpp -20.3 20.3 -38.1 38.1 6.3325 6.65  
 c square of moderator  
 2 rpp -19.9824 19.9824 -6.2 33.8 2.5124 6.3324  
 c moderator

3     rpp -19.9824 -16.4774 -6.2 33.8 -6.052 2.5124  
c   moderator

4     rpp 16.4774 19.9824 -6.2 33.8 -6.052 2.5124  
c   moderator

5     rpp 10.4574 16.4774 -6.2 33.8 1.8774 2.5124  
c   moderator

6     rpp -16.4774 -10.4574 -6.2 33.8 1.8774 2.5124  
c   outside of cylinder of moderator

7     rcc 0 17.8 -6.052 0 0 8.5644 9.525  
c   inside of cylinder of moderator

8     rcc 0 17.8 -6.052 0 0 8.5644 8.67375  
c   outside of aluminum cylinder, in contact with moderator

9     rcc 0 17.8 0.5039 0 0 1.27 15.1765  
c   inside of aluminum cylinder, in contact with moderator

10    rcc 0 17.8 0.5039 0 0 1.27 12.7635  
c   outside of aluminum cylinder (thinner), in contact with moderator

11    rcc 0 17.8 -8.3861 0 0 8.89 13.9065  
c   inside of aluminum cylinder (thinner), in contact with moderator

12    rcc 0 17.8 -8.3861 0 0 8.89 12.7635  
c   outside of aluminum cylinder (thicker)

13    rcc 0 17.8 -30.2555 0 0 21.8694 15.1765  
c   inside of aluminum cylinder (thicker)

14    rcc 0 17.8 -28.3505 0 0 19.9644 12.7635  
c   target: copper/water mix

15    rcc 0 17.8 2.5759 0 0 0.3175 1.905  
c   target: copper

16    rcc 0 17.8 2.5124001 0 0 0.381 3.81  
c   target: titanium

17    rcc 0 17.8 1.62339 0 0 0.889 2.2225  
c   outside of aluminum skirt around target

18    rcc 0 17.8 0.03589999 0 0 2.4765 6.2992



c inside of aluminum skirt around target

19 rcc 0 17.8 0.03589999 0 0 2.4765 2.2225001

c Aluminum cover - top

20 rpp -20.6175 20.6175 38.1 38.4175 -6.685 6.65

c Aluminum cover - bottom

21 rpp -20.6175 20.6172 -38.4175 -38.1 -6.685 6.65

c Aluminum cover - side

c 22 rpp -20.6175 -20.3 -38.4175 38.4175 -6.685 6.65

22 rpp -20.6175 -20.3 -38.1 38.1 -6.685 6.65

c Aluminum cover - side

c 23 rpp 20.3 20.6175 -38.4175 38.4175 -6.685 6.65

23 rpp 20.3 20.6175 -38.1 38.1 -6.685 6.65

c Aluminum cover - backplate

c 24 rpp -20.6175 20.6175 -38.4175 38.4175 -7.002501 -6.685

24 rpp -20.6175 20.6175 -38.1 38.1 -7.002501 -6.685

25 rcc 0 17.8 -7.1 0 0 0.6 15.2

c Cutout of backplate

c 25 rcc 0 17.8 -7.0025 0 0 0.3175 15.2

c The world

200 sph 0 0 0 500

c \*\*\*\*\*phantoms\*\*\*\*\*

c phantom containing water

c 15 rpp 15 18 -1.5 1.6 -17.3 -14

c tissue

c 15 rpp 9 21 -5 5 -14.31 -13.81

c changed y from -23 -14 to -5 5

c bone

c 16 rpp 9 21 -5 5 -15.32 -14.32

c skin

c 17 rpp 9 21 -5 5 -15.83 -15.33

c \*\*\*\*\*

```

c *****
c cutaway box for creating a cross sectional view
c 62    rpp -34 63 0.1 36 -36 36
c *****Test Object*****
c 153    s 15 0 -22 1
c *****additional moderator*****
c 154    rpp 9.1 21.1 -5 5 -20.5 -14
26    pz 6.66 $cell 16
27    pz 12.16 $cell 16
28    px 9.525 $cell 17
29    px -9.525 $cell 17
30    py 12.72 $cell 17
31    py 22.85 $cell 17
32    pz 12.17 $cell 17
33    pz 12.295 $cell 17
34    py 12.597
35    py 12.719
36    pz 22.33
37    py 22.851
38    pz 25.77
39    px 9.5251
40    px 40.6175 $60
41    py 12.596
42    pz 25.771
43    pz 59.871
44    px -40.62 $60
45    py 38.42
46    py 71.02
47    pz -110.2555
48    py 73.02
49    px -20.62

```

50 px -20.32  
 51 py 12.718  
 52 pz 11.98  
 54 c/z 0 17.8 4.25  
 55 pz 13.295  
 305 pz -70.2555  
 56 pz 30.42  
 57 pz -50.42  
 58 py 40.42  
 59 pz -10.42  
 60 pz 32.42  
 61 pz -52.42  
 62 pz -12.42  
 63 py 42.42  
 64 px 40  
 65 px 38  
 66 px -40  
 67 px -38  
 68 py 44.02  
 69 py 75.02  
 70 py 76.62  
 71 py 77.62  
 73 py -39  
 74 px -40.62  
 75 pz 12.5

mode n p e

m136 1001.70c -0.1118322 \$water phantom with 0.02 g Al

8016.70c -0.8875016 13027.70c -0.0006662225

m208 13027.70c -1 \$aluminum

m111 5010.70c -0.199 \$boron-10

5011.70c      -0.801  
 m209 29063.70c      0.6915 \$natural copper  
      29065.70c      0.3085  
 m317 1001.70c      0.333 \$copper and water mixture  
      8016.70c      0.167 29063.70c      0.34575 29065.70c      0.15425  
 m236 6000.70c      -1 \$graphite  
 c Titanium, changed 22050 from 0.056332 to 0.05633  
 m498 22046.70c      -0.076779 \$Titanium density 4.506 g/cm3  
      22047.70c      -0.071584 22048.70c      -0.739078 22049.70c      -0.056228  
      22050.70c      -0.056331  
 m1 1001.70c      -0.101172 \$soft tissue ICRU 4 component density=1.0 g/c  
      6000.70c      -0.111 7014.70c      -0.02790536 7015.70c      -9.464e-005  
      8016.70c      -0.7616075 8017.70c      -0.0002205451  
 c aluminum added to bone, replacing calcium  
 c total amount of Al added = 0.00666 grams (for optimization purposes)  
 c cortical bone ICRP density = 1.85 g/cc  
 m2 1001.70c      -0.04722697 \$0.00666 g Al  
      1002.70c      -7.356273e-006 3006.70c      -2.389742e-009  
 c MODERATORS  
 m256 1001.70c      -0.143711 \$polyethylene  
      6000.70c      -0.856289  
 m333 1001.70c      -0.1005977 \$30% by weight borated polyethylene p=1.19 g/cm3  
      6000.70c      -0.5994023 5010.70c      -0.0588 5011.70c      -0.2412  
 m434 1001.70c      -0.148605 \$paraffin wax p=0.93  
      6000.70c      -0.851395  
 m444 1001.70c      -0.1365255 \$5% by weight borated polyethylene p=1.08 g/cm3  
      6000.70c      -0.8134745 5010.70c      -0.0098 5011.70c      -0.0402  
 m228 1001.70c      -0.005558 \$concrete (ordinary with ENDF-VI), 2.35  
      8016.70c      -0.498076 11023.70c      -0.017101 12024.70c      -0.001999  
      12025.70c      -0.000264 12026.70c      -0.000302 13027.70c      -0.045746  
      14028.70c      -0.289486 14029.70c      -0.015181 14030.70c      -0.010425

```

16032.70c -0.001216 16033.70c -1e-005 16034.70c -5.7e-005
19039.70c -0.01788 19040.70c -2e-006 19041.70c -0.001357
20040.70c -0.08019 20042.70c -0.000562 20043.70c -0.00012
20044.70c -0.00188 20046.70c -4e-006 20048.70c -0.000186
26054.70c -0.000707 26056.70c -0.01139 26057.70c -0.000265
26058.70c -3.6e-005
m229 1002.70c -0.201133 $heavy water, 1.105340
8016.70c -0.798867
m230 1001.70c -0.111894 $light water, 0.998207
8016.70c -0.888106
m231 4009.70c -0.36032 $beryllium oxide, 3.010000
8016.70c -0.63968
m232 1001.70c -0.017371 $zirconium hydride zr5h8, 5.61
40000.70c -0.982629
m233 1001.70c -0.02162 $zirconium hydride zrh2, 5.61
40000.70c -0.97838
m234 23000.70c -1 $vandium, 6.11
m235 8000.70c -0.470749 $aluminum oxide, 3.97
13027.70c -0.529251
c end MODERATORS
m252 82206.70c -0.242902 $lead density = 11.35 g/cm3
82207.70c -0.223827 82208.70c -0.53327
m204 7014.70c -0.7528855 $air (US S. Atm at sea level)
7015.70c -0.002750515 8016.70c -0.231387 8017.70c -8.79605e-005
18036.70c -3.9e-005 18038.70c -8e-006 18040.70c -0.012842
c
c Start Phantoms
c
c 10,000 ppm fm4 Mg = 2.858638E-04, fm4 Ca = 3.326481E-03
c 4,000 ppm fm4 Mg = 1.143455E-04, fm4 Ca = 3.433617E-03
c 2,000 ppm fm4 Mg = 5.717275E-05, fm4 Ca = 3.469329E-03

```

c 1,000 ppm fm4 Mg = 2.858638E-05, fm4 Ca = 3.487185E-03  
 c 500 ppm fm4 Mg = 1.429319E-05, fm4 Ca = 3.496113E-03  
 c 100 ppm fm4 Mg = 2.858638E-06, fm4 Ca = 3.503255E-03  
 c 50 ppm fm4 Mg = 1.429319E-06, fm4 Ca = 3.504148E-03  
 c 0 ppm fm4 Mg = 0.000000E+00, fm4 Ca = 3.505041E-03  
 m300 1001.70c -0.021925 \$Phantom, 10K  
     7014.70c -0.00501 11023.70c -0.006382 20040.70c -0.21477  
     16032.70c -0.184994 8016.70c -0.554119 17035.70c -0.0028  
     12024.70c -0.01 20048.70c -0.000402  
 m301 1001.70c -0.022621 \$Phantom, 4K  
     7014.70c -0.00501 11023.70c -0.006382 20040.70c -0.221687  
     16032.70c -0.182613 8016.70c -0.554888 17035.70c -0.0028  
     12024.70c -0.004 20048.70c -0.000415  
 m302 1001.70c -0.022853 \$Phantom, 2K  
     7014.70c -0.00501 11023.70c -0.006382 20040.70c -0.223992  
     16032.70c -0.181819 8016.70c -0.555144 17035.70c -0.0028  
     12024.70c -0.002 20048.70c -0.000419  
 m303 1001.70c -0.022969 \$Phantom, 1K  
     7014.70c -0.00501 11023.70c -0.006382 20040.70c -0.225145  
     16032.70c -0.181422 8016.70c -0.555272 17035.70c -0.0028  
     12024.70c -0.001 20048.70c -0.000421  
 m304 1001.70c -0.023027 \$Phantom, 500  
     7014.70c -0.00501 11023.70c -0.006382 20040.70c -0.225722  
     16032.70c -0.181223 8016.70c -0.555336 17035.70c -0.0028  
     12024.70c -0.0005 20048.70c -0.000422  
 m305 1001.70c -0.023073 \$Phantom, 100  
     7014.70c -0.00501 11023.70c -0.006382 20040.70c -0.226183  
     16032.70c -0.181065 8016.70c -0.555388 17035.70c -0.0028  
     12024.70c -0.0001 20048.70c -0.000423  
 m306 1001.70c -0.023079 \$Phantom, 50  
     7014.70c -0.00501 11023.70c -0.006382 20040.70c -0.226241

16032.70c	-0.181045	8016.70c	-0.555394	17035.70c	-0.0028
12024.70c	-5e-005	20048.70c	-0.000423		
m307 1001.70c	-0.023085	\$Phantom, 0			
7014.70c	-0.00501	11023.70c	-0.006382	20040.70c	-0.226298
16032.70c	-0.181025	8016.70c	-0.5554	17035.70c	-0.0028
20048.70c	-0.000423				
c					
c End Phantoms					
c					
m308 12026.70c	-1				
m309 20048.70c	-1				
m999 7014.70c	-0.7528855	\$air (1e-4 torr pressure)			
7015.70c	-0.002750515	8016.70c	-0.231475	8017.70c	-8.79605e-005
18036.70c	-3.9e-005	18038.70c	-8e-006	18040.70c	-0.012842
c Steel					
m1000 6000.01p	-0.00075	\$Steel			
7014.70c	-0.00125	14000.60c	-0.005	15031.70c	-0.0003
16000.62c	-0.00015	24000.42c	-0.18	25055.70c	-0.0875
26000.55c	-0.67505				
m492 6000.70c	-0.002	\$Steel, HT9 Stainless,			
14028.70c	-0.003675	14029.70c	-0.000193	14030.70c	-0.000132
15031.70c	-0.0003	16032.70c	-0.000189	16033.70c	-2e-006
16034.70c	-9e-006	23000.70c	-0.003	24050.70c	-0.004799
24052.70c	-0.096256	24053.70c	-0.011123	24054.70c	-0.002821
25055.70c	-0.006	26054.70c	-0.048409	26056.70c	-0.780435
26057.70c	-0.018188	26058.70c	-0.002468	28058.70c	-0.00337
28060.70c	-0.001333	28061.70c	-5.9e-005	28062.70c	-0.000189
28064.70c	-5e-005	42092.70c	-0.001422	42094.70c	-0.000905
42095.70c	-0.001575	42096.70c	-0.001668	42097.70c	-0.000965
42098.70c	-0.002463	42100.70c	-0.001003	74183.70c	-0.005
m524 1001.70c	-0.057889	\$Southern Pine Wood, -.64			

6000.70c -0.482667 8016.70c -0.459444  
 m468 1001.70c -0.048382 \$Polyvinyl Chloride, 1.406  
 6000.70c -0.384361 17035.70c -0.423941 17037.70c -0.143316  
 imp:n 1 3r 0 1 37r \$ 1, 48  
 imp:p 1 3r 0 1 37r \$ 1, 48  
 imp:e 1 3r 0 1 37r \$ 1, 48  
 mt208 al27.12t  
 mt236 grph.10t  
 mt256 poly.10t  
 mt229 hwtr.10t \$for heavy water  
 mt230 lwtr.10t \$for light water  
 mt231 be/o.10t \$for BeO  
 mt232 h/zr.10t \$for zirconium hydride  
 mt233 h/zr.10t \$for zirconium hydride  
 phys:n 20 20 0  
 phys:p 100 0  
 phys:e 100 0  
 c act fission=n nonfiss=none dn=prompt dg=mg thresh=1.0 nap=1000  
 sdef erg=2.45 par=1 pos=0 17.8 2  
 c \*\*\*\*\*  
 c flux over a cell tally  
 c \*\*\*\*\*  
 fc4 Net Count tally  
 f4:n 29  
 c e4:n 1e-8 100ILOG 2.5 \$100i  
 fm4 261012.443 308 102  
 sd4 1  
 fc14 Phantom Dose Tally  
 f14:n 29  
 df14 IU=2 IC=20  
 fc24 Test Dose



f24:p 29

df24 IU=2 IC=20

f34:n 29

fm34 30933.8365 309 102 \$"calcium"

sd34 1

nps 5e6

## HPGE INPUT FILE

MCNPX Visual Editor Version X\_24E

c Created on: Tuesday, August 22, 2017 at 11:04

```

1  1  -5.32 -2 4 -3 (32 :11 :-33 )#17 #15 #14 #40 #41 $Ge
2  208 -2.6989 18 -6 11 -46 102 $Al
3  208 -2.6989 102 45 -46 -18
5  458  -1.38 5 -4 -46 -102 $mylar
500 208 -2.6989 -5 500 -46
6  208 -2.6989 47 -48 -23 12
7  0    -45 102 -18 (52 :3 )
8  0    -23 -47 12 (6 :46 :-500 )
9  0    18 -6 -11
10 204 -0.001225 -1 (-13 :23 :48 :55 )#19 #20 #21 #22 #23 #24 #25 #26 #27
    #28 #29 #30 #31 #32 #33 #34 #35 #36 #37 #42 #43 #44
11 0    1
14 0    -49 -3 (-50 :51 )
15 0    -52 102 53 -34 (36 :-35 :38 :-37 :41 :-40 :43 :-44 )
16 208 -2.6699 -12 13 -48
17 1  -5.32 -3 -11 (-32 :19 )#14 $dead layer, inner
18 1  -5.32 2 -52 (-33 :-3 )#40 #15 #8 #16 $dead layer, outer crista
    #10 #500 #5 #42 #43
19 208 -2.6989 23 -55 -56 (57 :54 :-58 )86
20 204 -0.001225 58 -54 -57
21 252 -11.35 13 -80 -90 89 84 -85
22 252 -11.35 80 -90 89 -81 84 -85

```

```

23 252 -11.35 81 -82 -90 89 84 -85
24 252 -11.35 82 -83 -90 89 84 -85
25 252 -11.35 79 -77 86 -87 13 -23
26 252 -11.35 79 -77 87 -88 13 -23
27 252 -11.35 79 -77 88 -89 13 -23
28 252 -11.35 79 -77 86 -87 23 -91
29 252 -11.35 79 -77 87 -88 23 -91
30 252 -11.35 79 -77 88 -89 23 -91
31 252 -11.35 76 -78 86 -87 13 -23
32 252 -11.35 76 -78 87 -88 13 -23
33 252 -11.35 76 -78 88 -89 13 -23
34 252 -11.35 76 -78 86 -87 23 -91
35 252 -11.35 76 -78 87 -88 23 -91
36 252 -11.35 76 -78 88 -89 23 -91
37 4 -0.64 -86 92 93 -94 95 -96
c 38 5 -2.23 -97 -98 86 (99 :100 :105 ) $phantom or source set
c 39 6 -1.033 -99 -100 -105 $ phantom or source set
40 1 -5.32 (-53 33 )(36 :-35 :38 :-37 :41 :-40 :43 :-44 )-34 -52 4
c 40 is the outer dead layer in the rounded region
41 1 -5.32 102 -52 -4 (-4 :-53 )#40 #15 $ dl on the top of the detec
42 300 -1.85 104 -13 -103
43 252 -11.35 107 (-106 :-77 :76 )-13 86 -89 79 -78 $lead shielding
44 252 -11.35 107 89 -90 -13 84 -85 $lead shielding at end of detect

1 so 100 $world
2 cx 3.775 $crystal
3 px 4.91 $crystal
4 px -4.24 $crystal
5 px -4.28 $Al/Mylar window
500 px -4.29
6 px 8.76 $Cup length

```

11 cx 0.7 \$inside cylinder  
12 px -4.643 \$Gap  
13 px -4.943 \$Al  
18 px 8.46 \$Al  
19 px -2.92  
23 px 15.207 \$fictional stop  
32 s -2.85 0 0 0.7  
33 tx -3.41 0 0 2.975 0.83 0.83  
34 px -3.41  
35 pz -2.975  
36 pz 2.975  
37 py -2.975  
38 py 2.975  
40 p 0 0.70710678859302 0.70710678859302 -2.99  
41 p 0 0.70710681270686 0.70710681270686 2.99  
43 p 0 0.70710678859302 -0.70710678859302 3  
44 p 0 0.70710678859302 -0.70710678859302 -3  
45 cx 4.2  
46 cx 4.28  
47 cx 4.7  
48 cx 4.85  
49 cx 0.5  
50 s -2.85 0 0 0.5  
51 px -2.85  
52 cx 3.79  
53 tx -3.41 0 0 2.975 0.855 0.855  
54 cx 5.5  
55 cx 5.6  
56 px 26.707  
57 px 26.607  
58 px 15.307

76 py 5.8  
77 py -5.8  
78 py 15.8  
79 py -15.8  
80 px 4.793  
81 px 14.793  
82 px 24.793  
83 px 34.793  
84 py -10  
85 py 10  
86 pz -5.6  
87 pz -0.85  
88 pz 3.9  
89 pz 8.65  
90 pz 13.4  
91 px 35.207  
92 pz -7.543  
93 px -30  
94 px 40  
95 py -30  
96 py 40  
97 c/z -5.944 0 1 \$-9.793 0 1  
98 pz 0.9  
99 c/z -5.944 0 0.95 \$\$-9.793 0 1  
100 pz -0.6  
101 pz -5.4  
102 px -4.27  
103 cx 4 \$phantom  
104 px -5.793  
105 k/z -5.944 0 -5.3 0.85 1  
106 px -7.2

107 px -11.75

mode p

m204 7000. -0.755636 \$air (US S. Atm at sea level)

8000. -0.231475 18000. -3.9e-005 18000. -8e-006

18000. -0.012842

m208 13000. -1 \$aluminum

m458 1000. -0.04196 \$Polyeth Terephthalate (Mylar),

6000. -0.625016 8000. -0.333024

c Germanium

m1 32000. -1 \$Germanium

c lithium

m21 3000. -0.1 \$lithium

32000. -0.9

c boron

m31 5000. -0.1 \$boron

32000. -0.9

m252 82000. -1 \$lead

m4 1000. -0.059642 \$wood, from pnnl, -0.64

6000. -0.497018 7000. -0.00497 8000. -0.427435

12000. -0.001988 16000. -0.00497 19000. -0.001988

20000. -0.001988

c Pyrex Glass, 2.23

m5 5000. -0.040064

8000. -0.539562 11000. -0.028191 13000. -0.011644

14000. -0.37722 19000. -0.003321

c HCl, 1.19 g/cm3

m6 1000. -0.02764674

17000. -0.9722984

m300 1001. -0.02132674 \$Phantom, 10K

7014. -0.01753001 11023. -0.01791878 20040. -0.1930784

16032.	-0.1636846	8016.	-0.5241159	17035.	-0.01673809
12024.	-0.04560757				
m301 1001.	-0.02238885	\$Phantom, 4K			
7014.	-0.01840304	11023.	-0.01881117	20040.	-0.202694
16032.	-0.1660356	8016.	-0.5349441	17035.	-0.01757168
12024.	-0.01915157				
m302 1001.	-0.0227668	\$Phantom, 2K			
7014.	-0.0187137	11023.	-0.01912872	20040.	-0.2061157
16032.	-0.1668721	8016.	-0.5387973	17035.	-0.0178683
12024.	-0.00973743				
m303 1001.	-0.02296059	\$Phantom, 1K			
7014.	-0.01887299	11023.	-0.01929155	20040.	-0.2078702
16032.	-0.1673011	8016.	-0.540773	17035.	-0.0180204
12024.	-0.004910159				
m304 1001.	-0.02305873	\$Phantom, 500			
7014.	-0.01895366	11023.	-0.01937401	20040.	-0.2087587
16032.	-0.1675183	8016.	-0.5417736	17035.	-0.01809742
12024.	-0.002465573				
m305 1001.	-0.02313785	\$Phantom, 100			
7014.	-0.0190187	11023.	-0.01944048	20040.	-0.209475
16032.	-0.1676935	8016.	-0.5425802	17035.	-0.01815952
12024.	-0.000494807				
m306 1001.	-0.02314778	\$Phantom, 50			
7014.	-0.01902686	11023.	-0.01944882	20040.	-0.2095648
16032.	-0.1677155	8016.	-0.5426814	17035.	-0.01816731
12024.	-0.000247509				
m307 1001.	-0.02315772	\$Phantom, 0			
7014.	-0.01903502	11023.	-0.01945717	20040.	-0.2096548
16032.	-0.1677375	8016.	-0.5427827	17035.	-0.01817511
imp:p 1 9r	0	1 28r	\$ 1, 44		
imp:e 1 9r	0	1 28r	\$ 1, 44		

```

c PTRAC file=asc max=1e7 nps=1,1e8 type=p event=src,col cell=1 write=all
nps 1e9
c f1:p 1
f8:p 1
e8 0 1e-5 1e-3 16383i 3.40196
c e1 0 1e-5 1e-3 16383i 3.40196
c ft8 geb -0.0007802 0.0606 1504 $ levenberg marquardt
c ft8 geb 0.0008644 0.0008052 0.7319 $ trust region
c ft1 geb 0.0008644 0.0008052 0.7319 $ trust region
c sdef pos= -5.944 0 -5.3 rad=d1 ext=d2 erg=d3 axs=0 0 1 cel=39
sdef pos= -5.593 0 -5.3 rad=d1 ext=d2 erg=d3 axs=0 0 1 cel=42
c si1 0 0.95
si1 0 1.3
sp1 -21 1
c si2 0 5
si2 0 10
sp2 0 1 $uniform probability over range
si3 1 0.087346 0.121755 0.660653 1.17149 1.33083
sp3 4.14521E-03 3.86156E-04 3.30370E-01 2.48221E-01 2.48519E-01
c sp3 D 0.00499059 0.000867342 0.377222216 0.307273704 0.307642949
prdmp 2j

```

## APPENDIX B. PHANTOM RECIPE

Table A.1 Phantom recipe for all concentrations

0 ppm		MgSO4	CaSO4	NH4Cl	NaNO3	Total			
Amount in phantom, g		0.000	60.271	0.262	1.467	62			
Element	Ca	Mg	S	O	N	H	Cl	Na	Total
Quantity of Each Element in Phantom, g	14.030	0.000	11.224	34.435	0.311	1.431	0.174	0.396	62
MCNP Input	-2.263E-01	0.000E+00	-1.810E-01	-5.554E-01	-5.010E-03	-2.308E-02	-2.800E-03	-6.382E-03	-1
50 ppm		MgSO4	CaSO4	NH4Cl	NaNO3	Total			
Amount in phantom, g		0.015	60.256	0.262	1.467	62			
Element	Ca	Mg	S	O	N	H	Cl	Na	Total
Quantity of Each Element in Phantom, g	14.027	0.003	11.225	34.434	0.311	1.431	0.174	0.396	62
MCNP Input	-2.262E-01	-5.000E-05	-1.810E-01	-5.554E-01	-5.010E-03	-2.308E-02	-2.800E-03	-6.382E-03	-1
100 ppm		MgSO4	CaSO4	NH4Cl	NaNO3	Total			
Amount in phantom, g		0.031	60.240	0.262	1.467	62			
Element	Ca	Mg	S	O	N	H	Cl	Na	Total
Quantity of Each Element in Phantom, g	14.023	0.006	11.226	34.434	0.311	1.431	0.174	0.396	62
MCNP Input	-2.262E-01	-1.000E-04	-1.811E-01	-5.554E-01	-5.010E-03	-2.307E-02	-2.800E-03	-6.382E-03	-1
500 ppm		MgSO4	CaSO4	NH4Cl	NaNO3	Total			
Amount in phantom, g		0.154	60.118	0.262	1.467	62			



Element	Ca	Mg	S	O	N	H	Cl	Na	Total
Quantity of Each Element in Phantom, g	13.995	0.031	11.236	34.431	0.311	1.428	0.174	0.396	62
MCNP Input	-2.257E-01	-5.000E-04	-1.812E-01	-5.553E-01	-5.010E-03	-2.303E-02	-2.800E-03	-6.382E-03	-1
1000 ppm		MgSO4	CaSO4	NH4Cl	NaNO3	Total			
Amount in phantom, g		0.307	59.964	0.262	1.467	62			
Element	Ca	Mg	S	O	N	H	Cl	Na	Total
Quantity of Each Element in Phantom, g	13.959	0.062	11.248	34.427	0.311	1.424	0.174	0.396	62
MCNP Input	-2.251E-01	-1.000E-03	-1.814E-01	-5.553E-01	-5.010E-03	-2.297E-02	-2.800E-03	-6.382E-03	-1
2000 ppm		MgSO4	CaSO4	NH4Cl	NaNO3	Total			
Amount in phantom, g		0.614	59.657	0.262	1.467	62			
Element	Ca	Mg	S	O	N	H	Cl	Na	Total
Quantity of Each Element in Phantom, g	13.888	0.124	11.273	34.419	0.311	1.417	0.174	0.396	62
MCNP Input	-2.240E-01	-2.000E-03	-1.818E-01	-5.551E-01	-5.010E-03	-2.285E-02	-2.800E-03	-6.382E-03	-1
4000 ppm		MgSO4	CaSO4	NH4Cl	NaNO3	Total			
Amount in phantom, g		1.228	59.043	0.262	1.467	62			
Element	Ca	Mg	S	O	N	H	Cl	Na	Total
Quantity of Each Element in Phantom, g	13.745	0.248	11.322	34.403	0.311	1.403	0.174	0.396	62
MCNP Input	-2.217E-01	-4.000E-03	-1.826E-01	-5.549E-01	-5.010E-03	-2.262E-02	-2.800E-03	-6.382E-03	-1
10000 ppm		MgSO4	CaSO4	NH4Cl	NaNO3	Total			
Amount in phantom, g		3.070	57.201	0.262	1.467	62			
Element	Ca	Mg	S	O	N	H	Cl	Na	Total

Quantity of Each Element in Phantom, g	13.316	0.620	11.470	34.355	0.311	1.359	0.174	0.396	62
MCNP Input	-2.148E-01	-1.000E-02	-1.850E-01	-5.541E-01	-5.010E-03	-2.193E-02	-2.800E-03	-6.382E-03	-1